Research Square

Preprints are preliminary reports that have not undergone peer review.
They should not be considered conclusive, used to inform clinical practice,
or referenced by the media as validated information.

Multi-Tiered Magmatic Plumbing System of the Tatun Volcano Group, Taiwan: Insights from Mineral Thermobarometry and Reservoir Evolution

Guo-Teng Hong

gthong@gsmma.gov.tw

Geological Survey and Mining Management Agency, MOEA

Kuo-Lung Wang

Academia Sinica

Yoshiyuki Iizuka

Academia Sinica

Cheng-Hong Chen

National Taiwan University

Yu-Shiang Wang

Academia Sinica

Cheng-Horng Lin

Academia Sinica

Yuan-Hsi Lee

National Chung Cheng University

Daniel P. Miggins

Oregon State University

Research Article

Keywords: Tatun Volcano Group, magma reservoir, geothermobarometry, amphibole decomposition, magma evolution, magmatism dynamics

Posted Date: October 7th, 2026

DOI: https://doi.org/10.21203/rs.3.rs-10933151/v1

License: This work is licensed under a Creative Commons Attribution 4.0 International License.
Read Full License

Additional Declarations: No competing interests reported.

Multi-Tiered Magmatic Plumbing System of the Tatun Volcano Group, Taiwan: Insights from Mineral Thermobarometry and Reservoir Evolution

Guo-Teng Hong[1,2]*, Kuo-Lung Wang[2,3], Yoshiyuki Iizuka[3,4], Cheng-Hong Chen[2], Yu-Shiang Wang[3], Cheng-Horng Lin[3], Yuan-Hsi Lee[5], Daniel P. Miggins[6]

[1]Geological Survey and Mining Management Agency, MOEA, Taipei, Taiwan

[2]Department of Geosciences, National Taiwan University, Taipei, Taiwan

[3]Institute of Earth Sciences, Academia Sinica, Taipei, Taiwan

[4]Graduate School of Arts and Letters, Tohoku University, Sendai, Japan

[5]Department of Earth and Environmental Sciences, National Chung Cheng University, Chiayi, Taiwan

[6]OSU Argon Geochronology Laboratory, College of Earth, Ocean, and Atmospheric Sciences, Oregon State University, Corvallis, USA

*Corresponding author

ORCID iD: 0009-0008-5952-1480

Email: gthong@gsmma.gov.tw

Version on 3 September 2026

Abstract

The potential reactivation of the Tatun Volcano Group (TVG) in northern Taiwan has raised significant public and geohazard concerns. To constrain magma stagnation depth and reconstruct the plumbing system architecture of the TVG, this study applies mineral thermobarometry to 33 core samples from four andesitic lava units (Lv1–Lv4) retrieved from a deep borehole at Mt. Tatun. Mineral chemistry and petrography reveal polybaric crystallization, stagnation, and mixing across multiple crustal levels. Magma evolution progressed from deep-crustal orthopyroxene crystallization to mid-to-shallow-crustal amphibole/clinopyroxene crystallization, depicting a crystal-stagnation ceiling at 4km. This evolution was accompanied by mixing of ascending mafic magmas and stagnated, amphibole-bearing intermediate magma batches. Prior to eruption, the stagnated magmas, initially in a highly crystallized lock-up state, were reactivated by replenished magma recharge, triggering multi-stage causing stepped amphibole decomposition (decompression rims and thermal oxidation) and promoting dominant feldspar microlite accumulation over fractionation. Amphibole decompression rims yield slow magma ascent rates of 0.004 to 0.011 m/s, consistent with the widespread distribution of effusive lava flows across the TVG. Comparing these petrological results with modern seismological data reveals that the paleo-reservoir spanned a wider range of magma-ponding depths (4-22 km). The dimensional retreat of the main reservoir from the late Pleistocene to the present (8-20 km) suggests a significant reduction of the TVG's magma volume, with the reservoir ceiling descending from 4 km to 8 km depth over 110 kys. The observed low-velocity magma ascent is linked to post-collisional crustal rebound and asthenosphere upwelling within the extensional regime of the Northern Taiwan Volcanic Zone. Although the modern, stable stress field implies a recessed magma supply relative to the Pleistocene, low-explosivity effusive activity remains a potential long-term threat. A known hydrothermal reservoir at 2–4 km depth may serve as the final staging area priming future magma extrusion.

Keywords:

Tatun Volcano Group, magma reservoir, geothermobarometry, amphibole decomposition, magma evolution, magmatism dynamics

1. Introduction

The active Tatun Volcano Group (TVG) in the Northern Taiwan Volcanic Zone (NTVZ) poses a significant safety risk due to its proximity to the Taipei metropolitan area (Fig. 1). Indirect evidence suggests the last TVG eruption within the 10,000 years (Zellmer et al. 2015; Belousov et al. 2010), while other studies point to ca. 10-20 ka (Chen & Lin 2000, 2002; Chen et al. 2010; Song et al. 2017; Jabagat et al. 2026). Recently, the use of cutting-edge dating techniques for young materials, such as the precise $^{40}Ar/^{39}Ar$ and Zircon Double-Dating (ZDD) on U-Th/He systems, has renewed the youngest TVG magmatic eruption record (ca. 8 ka) in the Holocene (Ignacio et al. 2026). The intact volcanic landforms, including lava domes, lava flows, and explosive craters (Chan e al. 2006; Chen et al. 2007; Song et al. 2011, 2021; Liao 2018), further support a short dormant period since the last unrest.

Using mineral thermobarometry (Putirka et al. 1996; Putirka 2008, 2017), this study aims to reconstruct the pressure–temperature evolution of TVG magmas, thereby characterizing magma migration dynamics from the reservoir to the surface in relation to the active plumbing system. Two significant features characterizing TVG's plumbing system are focused: (1) previous magma stagnation depths (proximity to the magma reservoir), compared to the present reservoir at depths of 8-20 km indicated by the teleseismic model (Lin 2016; Huang et al. 2021), and (2) magma ascent rate (Geschwind & Rutherford 1995; Rutherford & Hill 1993; Rutherford & Devine 2003; Nakamura 1995; Klügel et al. 1997; Rutherford 2008), which reflects previous eruptive style − explosive or effusive (Sparks et al. 1998; Rutherford, 2008) − and informs future hazard potential.

Given the uncertainties in teleseismic models, which depend on presumed heterogeneous factors such as temperature, composition, and fluid proportion in the crust (Lin 2016; Huang et al. 2021), petrography and mineral thermobarometry provide additional constraints on the TVG's reservoir and magma evolution (Putirka et al. 1996; Putirka 1997; Putirka & Condit

2003; Klügel & Klein 2005; Yang et al. 1996; Ridolfi et al. 2010; Nagasaki et al. 2017). By estimating the magma's physical conditions from crystal chemistry, the dimensions and location of the TVG magma reservoir can be examined. Lastly, this study assesses the persistence of TVG magmatism through the lens of magmatic dynamics, using local structural evidence, such as stress field distributions, to evaluate future eruptive potential.

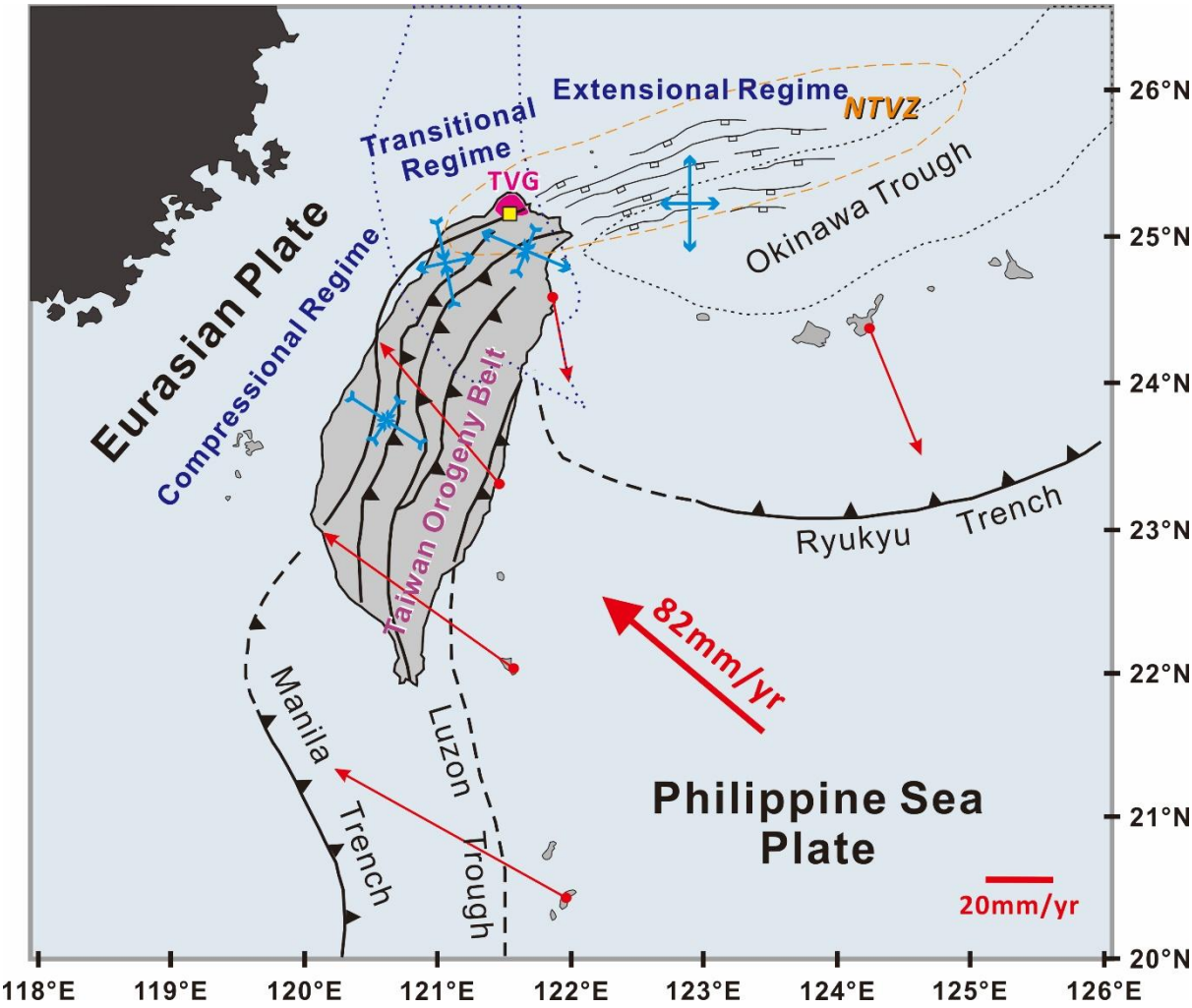


Fig. 1_Regional tectonic setting of Taiwan and its neighboring area (summarized from Kong et al. 2000; Hu et al. 2002; Hsu et al. 2009). Taiwan, formed by the collision of the Philippine Sea Plate and the Eurasian Plate, sits at the junction of two subduction systems, the Ryukyu Trench to the east and the Manila Trench to the south. The Tatun Volcano Group (TVG), located in the southwestern part of the northern Taiwan volcanic zone (NTVZ), poses a significant risk due to its proximity to Taipei City. The TVG lies in a transitional stress regime

with a very low strain rate, between the compressional tectonic regime in the south and the extensional tectonic regime in the northeast (where NTVZ developed) (Hu et al. 2002). Red arrows represent the vectors of relative plate motion. Pairs of convergent and divergent arrows (blue) indicate the maximum compressive and minimum extensional stresses, respectively (Hu et al. 2002; Hsu et al. 2009).

2. Geological Background

2.1. Tectonic setting and petrogenesis of TVG magmas

The TVG in northern Taiwan comprises intermediate-composition volcanoes formed in a post-collisional rifting system (Wang et al. 2004; Shellnutt et al. 2014) (Fig. 1). Since the Pliocene, convergence between the Eurasian and Philippine Sea plates had shaped a NE-trending fold-and-thrust belt composed of the Wutsishan, Mushan, Taliao, Shihti, Nanchuang, and Kueichulin formations, transected by the Kanchiao and Shinchuang faults (Fig. 2). In the late Pleistocene, post-orogenic extensional rifting induced tectonic subsidence and TVG magmatic activity along the Shanchiao fault. This volcanic suite ranges from calc-alkaline basaltic andesites to andesites, with minor continental margin-type high-alumina basalts (Chen 1975, 1978a). Compositional variation of the TVG and other volcanoes' magmas in NTVZ is attributed to partial melting of the asthenospheric mantle then contaminated by subcontinental lithospheric mantle, driven by asthenosphere upwelling during post-collisional extension (Wang et al. 2004; Shellnutt et al. 2014). MELTS modeling suggests that TVG basaltic andesite magma is derived from partial melting of mantle pyroxenite, followed by fractional crystallization to produce andesite magma (Shellnutt et al. 2014).

Basaltic andesites and andesites in the TVG have phenocrysts including plagioclase, orthopyroxene, clinopyroxene, hornblende, and magnetite. Phenocryst assemblages characterize andesite types, such as two-pyroxene andesite, two-pyroxene hornblende andesite, hornblende two-pyroxene andesite, hornblende andesite, etc. (Chen & Wu 1971;

Chen 1975; Chen et al. 2003, 2007; Song et al. 2011). Four synthems (unconformity-bounded units for volcanic strata: Martí et al., 2018; Lucchi, 2019), namely the Chutze, Tatun, Chihsing-Huangtsui, and Tinghuohsiu-Nantze, are defined (Fig. 2) based on spatial distribution and volcanic topographic features of extrusive lava units in relation to andesite types, with eruption ages mostly overlapping within 1Ma (Age distribution refers to Supplementary Fig. S1).

The TVG features at least 51 volcanic cones − comprising composite volcanoes, parasitic cones, and lava domes − with characteristic landforms of explosion craters, lava flows, volcanic avalanches, and lahars (Chan et al. 2005; Chen et al. 2007; Song et al. 2011; Belousov et al. 2010). Age differences among the volcanoes disclose the eastern and northern parts of the TVG (Tinghuohsiu-Nantse and Chutse synthems) have undergone longer exhumation associated with earlier activities (> ca. 0.2 Ma, detailed in Supplementary Fig. S1), leaving residual volcanic landforms (Kear 1957; Hong 2014). In contrast, the central (Chihsing-Huangtsui synthem) and western (Tatun synthem) parts retain intact volcanic topography, e.g., craters and lava flows, reflecting recent activity and less exhumation (Song et al. 2021; Liao 2018; Chen et al. 2003, 2007).

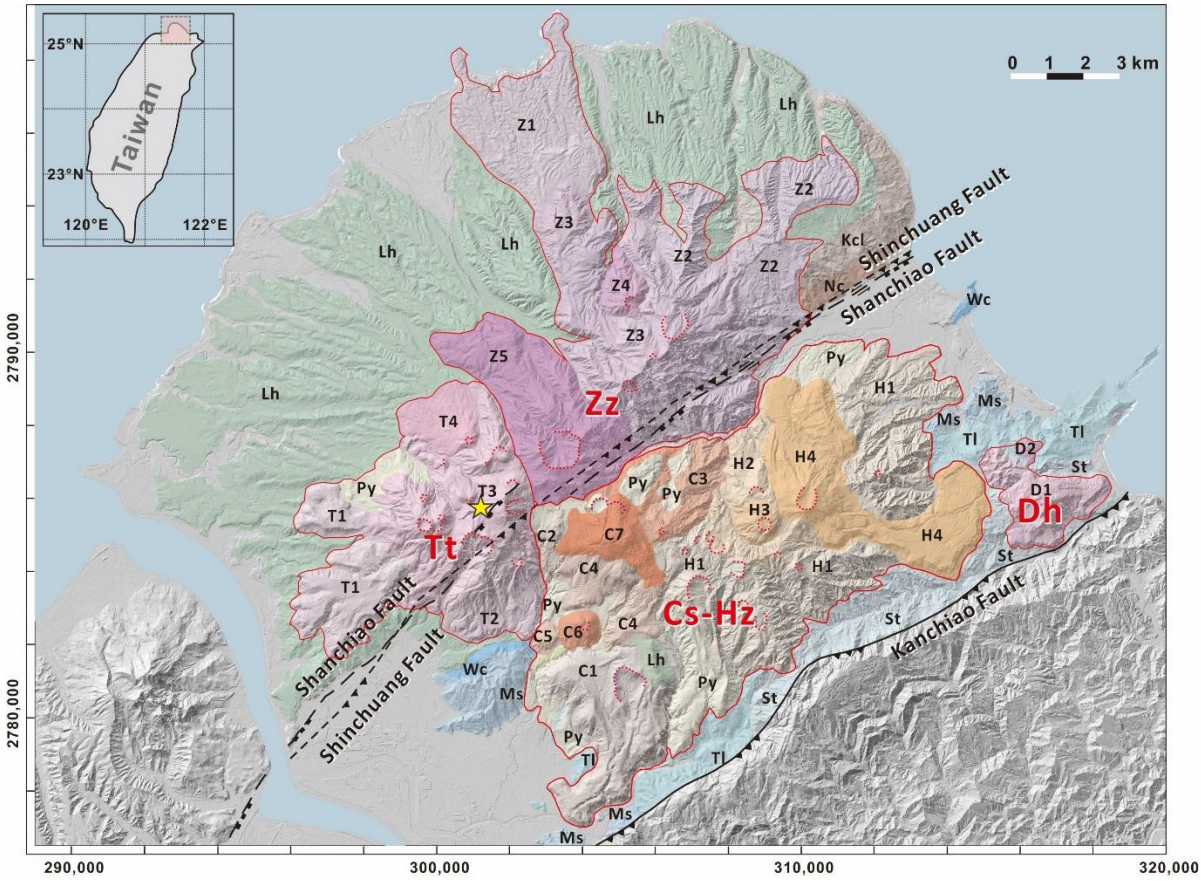


Fig. 2_The Tatun Volcano Group (TVG) is divided into four synthems (unconformity-bounded units for volcanic strata: Chang 1975; Marti et al. 2018; Lucchi et al. 2019): Chutze (Zz), Tatun (Tt), Chihsing-Huangtsui (Cs-Hz), and Tinghuohsiu-Nantze (Dh). The Shanchiao Fault separates the TVG into northwestern (Chutze and Tatun synthems) and southeastern (Chihsing-Huangtsui and Tinghuohsiu-Nantze synthems) parts. Each synthem comprises several overlapping volcanoes composed of andesitic-to-basaltic-andesitic lava domes, lava flows, volcanic avalanches, and vast flooded lahars (Lh). The numbering of each lithosome (e.g., T1, T2, T3) indicates its eruptive order within the synthem. The sedimentary basement exposed along the southeastern fringe of the TVG comprises Oligocene-to-Miocene strata, including the Wutsishan (Wc), Mushan (Ms), Taliao (Tl), and Shihti (St) Formations. The studied core, DT-01 (yellow star), is located at Mt. Tatun within the Tatun synthem (Tt).

2.2. Eruptive history

Initial determinations of TVG ages using the K-Ar (Juang & Bellon 1984; Juang & Chen 1989; Juang 1993; Tsao 1994) and Ar-Ar (Lee 1996) methods on surface volcanic rocks indicated that the TVG's eruptive period spanned from 2.56 to 0.19 Ma. Wang & Chen (1990) employed zircon fission-track dating to obtain ages ranging from 2.80 to 0.29 Ma. Notably, most samples yielded ages younger than 1 Ma. Chu et al. (2018) revisited age determination by analyzing zircon U-Pb ages from surface volcanic rocks, suggesting that the TVG's main eruptive period lay within 0.8 Ma, with a magmatic surge younger than 0.35 Ma.

While the TVG mainly erupted in the Late Pleistocene, recent evidence shows that its volcanic activity persisted into the Holocene, with a possible unrest occurring at Mt. Chihsing ca. 6 ka (Belousov et al. 2010). A magnetite crystallization age of 1,370 years by U/Th-Ra method from a lava dome near Mt. Chihsing (Zellmer et al. 2015) is questionable due to failed data replication (Song et al., 2017). Jabagat et al. (2026) redated the matrix and zircon grains of the lava dome, yielding $^{40}Ar/^{39}Ar$ age of 15±6.3 Ka and U-Th/He (zircon double dating) age of 16.3±4.9 Ka, respectively. Recently, Ignacio et al. (2026) reported multiple Holocene extrusive events at Mt. Chihsing, yielding a weighted mean eruption age ($^{40}Ar/^{39}Ar$ and ZDD) of 8.71±0.39 ka. This finding reveals that Holocene eruptions in the TVG have been underestimated.

3. Samples and Methods

3.1. Sample description

Regarding the concern about missing geological records due to surface exhumation, drilling cores preserve more robust eruption records than surface outcrops and better illustrate temporal changes in magmatic activity. A drilling core, DT-01, from Mt. Tatun (Fig. 2), stored by the Geological Survey and Mining Management Agency (GSMMA), provides ideal material for this study.

The DT-01 core (Fig. 3) is dominated by thick laharic deposits interbedded with massive

andesitic lavas. Four lava units, namely Lv1, Lv2, Lv3, and Lv4, in ascending order, are present. They are composed of andesite to basaltic andesite and commonly exhibit porphyritic textures. Fresh samples from each lava unit were collected at evenly spaced intervals for petrographic, mineral-chemical, and bulk-rock major-element analysis (Tab. 1-1). The stacking sequence of the lava units in the drilling core is straightforward, i.e., their eruptive order is well-constrained, which supports further discussion of temporal and spatial variations during magma crystallization.

Table 1-1_DT-01 sample list with phenocryst proportions for each sample. Sample numbering represents core depth in cm. Voids are ignored. Plg: plagioclase, Cpx: clinopyroxene, Opx: orthopyroxene, Amp: amphibole, Mgt: magnetite, Gm: groundmass. Mineral proportions are given in vol%. #Samples selected for whole-rock major-element composition analysis. *Samples from locations where $^{40}Ar/^{39}Ar$ dating ages were obtained.

DT-01 (cm)	Plg	Cpx	Opx	Amp	Mgt	Gm
			Lv-4			
*4700	39	1	5	6	< 1	49
5510	35	6	1	12	1	44
6390	40	3	1	4	< 1	52
7000	38	3	1	5	3	51
7880	19	9	1	9	1	61
*8600	26	2	1	8	< 1	62
9500	32	2	4	5	< 1	57
#10300	30	4	2	3	< 1	60
10990	28	3	1	9	1	58
11820	31	1	1	7	< 1	59
12500	55	0	7	11	4	22
13390	31	1	2	7	2	56
14100	31	2	5	5	1	56
15090	28	4	5	4	< 1	58
15890	32	8	0	3	< 1	58
16785	30	5	2	11	< 1	51
#17300	25	3	3	5	< 1	63
			Lv-3			
#18685	41	5	3	3	< 1	46
18875	33	5	3	5	1	52

			Lv-2			
#20740	8	7	1	1	< 1	82
*21520	32	1	4	5	3	56
22290	8	3	5	1	5	78
22930	34	2	3	2	< 1	60
23230	22	2	1	1	< 1	74
23600	30	1	4	1	< 1	64
			Lv-1			
34190	31	6	3	1	< 1	58
34985	32	6	5	1	< 1	55
#35640	35	6	4	1	5	50
36310	31	7	3	1	1	57
36930	25	7	4	1	< 1	63
37640	37	7	2	0	2	52
38270	27	5	4	0	1	62
#38655	28	5	2	3	1	62

187 Table 1-2_Summary of $^{40}Ar/^{39}Ar$ dating results for DT-01 samples.

Depth (cm)	Unit	Analyte	Age Type	Age (ka)	±2σ (ka)	K/Ca	±2σ	MSWD
9000	Lv 4	Groundmass	Plateau	140.4	6.1	0.397	0.019	0.34
21000	Lv 2	Groundmass	Plateau	474.4	10	0.624	0.021	0.88

188

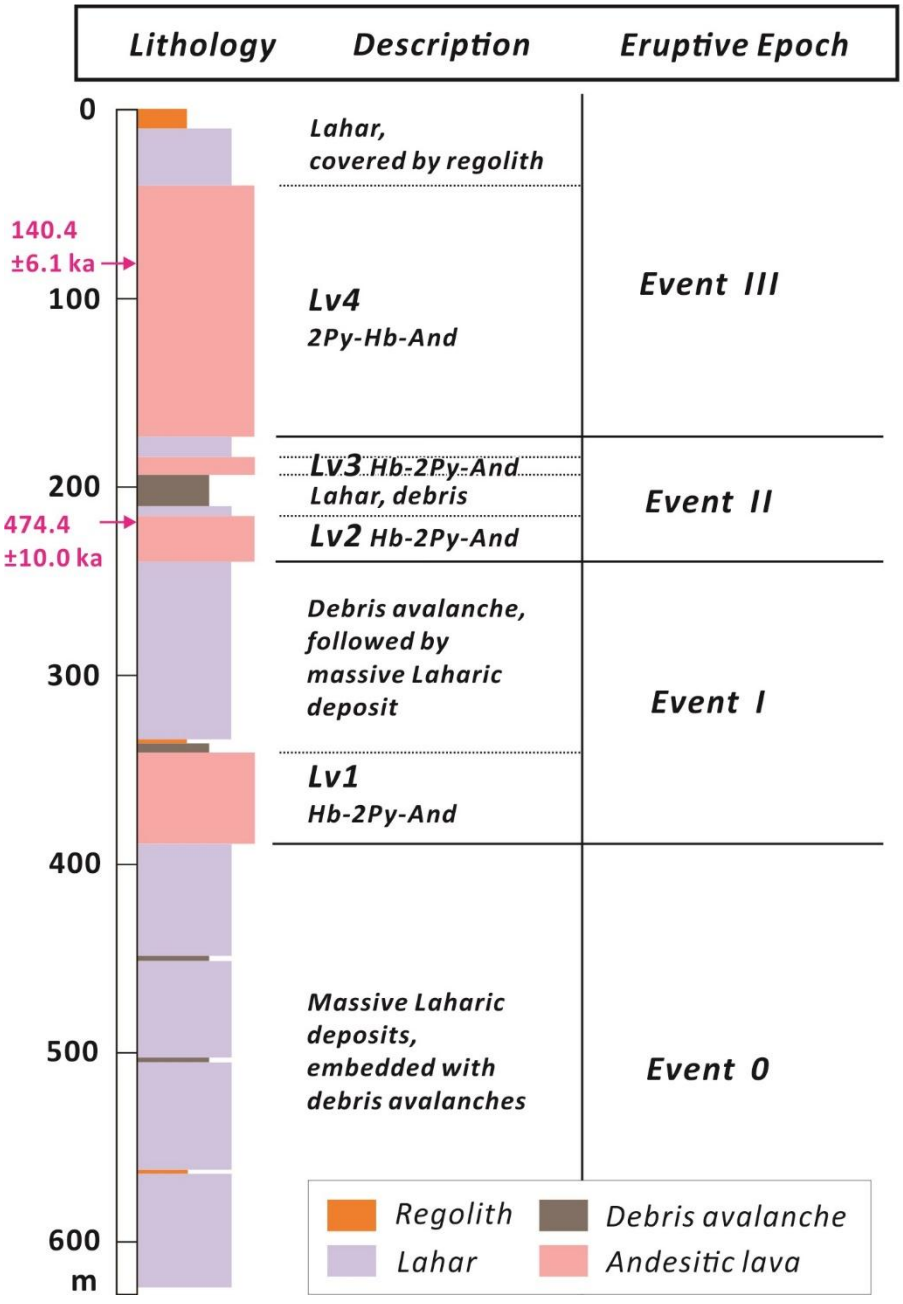


Fig. 3_Drilling core DT-01 lithologic column (see Fig. 2 for drilling core locality). It consists of massive laharic deposits, lava, and a few debris avalanches in alternation. At least four eruptive events are recorded in the section. Four andesitic lava units, namely Lv1 (hornblende two-pyroxene andesite), Lv2 (hornblende two-pyroxene andesite), Lv3 (hornblende two-pyroxene andesite), and Lv4 (two-pyroxene hornblende andesite) in ascending order, are associated with events I, II, and III. $^{40}Ar/^{39}Ar$ dating of lava groundmass at depths of 90 m (Lv4) and 214 m (Lv2) yields cooling (eruption) ages of 140 ka and 474 ka, respectively.

198 **3.2. Methods**

199 A total of 33 samples (Tab. 1-1) were collected from the four lava units, Lv1, Lv2, Lv3,
200 and Lv4, in the drilling core DT-01 (Fig. 3), which was obtained from the western part of the
201 TVG (Fig. 2). Thin sections for petrographic study were prepared for all samples by carefully
202 cutting to retain only the fresh portions. Phenocrysts and textures were examined under an
203 optical microscope and then a scanning electron microscope. Six representative samples from
204 the four lava units were analyzed for whole-rock compositions. In addition, $^{40}Ar/^{39}Ar$ ages for
205 two DT-01 lava samples were reported for discussion in the following sections (Fig. 3).
206
207 **3.2.1 $^{40}Ar/^{39}Ar$ Dating**

208 $^{40}Ar/^{39}Ar$ dating records the time since a rock last cooled below the Ar closure
209 temperature, marking the eruption age. Two samples (DT-01_9000, 21400) from Lv2 and Lv4
210 (Fig. 3) were sent to the argon geochronology laboratory at Oregon State University, US, for
211 groundmass analysis. Groundmass was separated to exclude inherited crystals, following
212 standard protocols (Koppers et al. 2000).

213 Samples were purified by acid leaching (HCl and HNO_3) and handpicked to >99.9%
214 purity. After one hour of irradiation with a Fish Canyon Tuff sanidine flux monitor, samples
215 were heated in an ultra-high-vacuum chamber using a stepped CO_2 laser beam to release
216 argon. Released gases were purified with Zr-Al getters, and argon isotopes were measured on
217 a multi-collector ARGUS-VI mass spectrometer. Final weighted-mean plateau and isochron
218 ages were calculated using ArArCALC v2.6.2 software (Koppers 2002), correcting for system
219 blanks, radioactive decay, mass discrimination, reactor-induced interferences, and
220 atmospheric contamination.
221
222 **3.2.2 Petrography and Mineral Chemistry**

223 The rock samples were mounted in epoxy resin and ground with SiC (silicon carbide)

papers from #400 to #2000 until a flat surface was achieved, then polished with 3μm and 1μm aluminum particulate compounds on rotary disks. The final polish was performed using a vibration polisher (Buhler: Vibromet-2) with a 0.3 μm alumina compound for several hours. The polished specimens were then coated with a carbon layer (Q150TE, Quorum Technologies Ltd., UK) to facilitate electron conductivity.

The micro-textures and chemistries of minerals were qualitatively examined using a scanning electron microscope (JEOL JSM-6360LV) at the Institute of Earth Sciences, Academia Sinica, Taiwan. Mineral identification was performed using an attached X-ray energy-dispersive spectrometer (EDS: Oxford Instruments Ltd., INCA-350) under beam conditions of 15 kV acceleration voltage and 0.2 nA current.

Mineral compositions were quantitatively determined using an electron probe micro-analyzer (JEOL EPMA JXA-8900R) equipped with five wavelength-dispersive spectrometers (WDS). Secondary- and back-scattered electron images were used to guide analysis of the mineral targets. A 2 μm defocused beam was used for quantitative analysis at an acceleration voltage of 15 kV and a beam current of 12 nA. Measured X-ray intensities were oxide ZAF-corrected using calibration of synthetic (s) and natural (n) standard minerals with various diffracting crystals, as follows: wollastonite (s) for Si with TAP crystal, rutile (s) for Ti with PETJ crystal, corundum (s) for Al (TAP), Cr-oxide (s) for Cr (PET), hematite (n) for Fe with LiFH crystal, Mn-oxide (s) for Mn (PET), periclase (s) for Mg (TAPH), wollastonite (s) for Ca (PETH), albite (n) for Na (TAPH), adularia (n) for K (PETH), and Ni oxide (s) for Ni (LiFH). Counting times were 10 seconds for each peak and 5 seconds for each upper and lower baseline for all elements. Standards run as unknowns yielded relative standard deviations below 1% for Si, Na, and K, and below 0.5% for other major elements. Based on 3σ of the standard calibration, the detection limits for all elements were 50-100 ppm.

3.2.3. Amphibole Occurrences

Amphibole decomposition from decompression during magma ascent is common in extrusive rocks (Rutherford 2008). The rim's growth rate and thickness depend on the decompression rate or path (Rutherford & Hill 1993; Rutherford & Devine 2003; Browne & Gardner 2006). Ideally, rim thickness can be used to estimate magma ascent rates (Rutherford & Hill 1993; Browne & Gardner 2006; McCanta et al. 2007; Rutherford 2008). Amphibole decomposes by magma decompression, thermal oxidation, and thermal recrystallization (Garcia & Jacobson 1979; DeAngelis et al. 2013). These mechanisms differ in mineral assemblage, grain size, and rim characteristics. Identifying the mechanism is crucial for using rim thickness to estimate ascent rates.

The amphibole decomposition mechanisms are characterized by the following:

Magma decompression (gabbroic-type): Decreased water fugacity dehydrates amphibole, producing pyroxene, titanomagnetite, and plagioclase (Garcia & Jacobson 1979) of 1-30 μm in size, forming rims <40 μm thick (DeAngelis et al. 2013). Pyroxene herein includes both clinopyroxene and orthopyroxene (Wright & Doherty 1970; Rutherford & Hill 1993; DeAngelis et al. 2013), though some report only orthopyroxene (Browne 2005). Decompression rims always form at the crystal-magma interface (Rutherford & Hill 1993), indicating magmatic reaction.

Thermal oxidation (black-type or opaque rim): Oxidation and dehydrogenation cause amphibole to decompose without magma involvement (Devine et al. 1998; Murphy et al. 2000; Garcia & Jacobson 1979). Such rims, <10 μm thick, are composed of clinopyroxene and titanomagnetite (Browne 2005), measuring 1-10 μm in size (DeAngelis et al. 2013).

Thermal recrystallization: When magma stalled in the shallow crust, amphibole transforms into pyroxene, titanomagnetite, and plagioclase (30-300 μm in size), forming broad rims >200 μm thick (Devine et al. 1998; Murphy et al. 2000; Rutherford & Devine 2003; DeAngelis et al. 2013). In DT-01 samples, this replacement often creates irregular patches.

Based on mass-balance estimates, the mineral transformation during amphibole decomposition is described by the reaction below (Wright & Doherty 1970; Rutherford & Hill 1993).

0.73 Amp + 0.27 melt = 0.29 Opx + 0.24 Cpx + 0.43 Plg + 0.03 Ilm (+ melt)

For magma components involved on both sides, the formula shows a mass imbalance between amphibole and decomposition phases and can be simplified as below (McCanta et al. 2007).

$Amp + melt_1 \rightarrow Opx + Cpx + Plg + Ilm + melt_2$

Amphibole decomposition during thermal oxidation and recrystallization has not been discussed in previous studies. Hence, we propose a mass-balance formula to explain amphibole breakdown without magma involvement.

Tschermakite Opx Cpx

$Ca_2(Mg,Fe^{2+,3+})_5Si_6Al_2O_{22}(OH)_2 \rightarrow (Mg,Fe)_2Si_2O_6 + (Ca,Mg,Fe^{3+},Al)_2(Si,Al)_2O_6 +$

Plg Mgt

$(Ca,Na)Al(Al,Si)Si_2O_8 + Fe^{2+}(Fe^{3+},Ti)_2O_4 + H_2 + Si$

Statistical analysis of amphibole textures at different core depths, combined with thermobarometry, reveals a stepped ascent in magma evolution. In addition to magma decompression, thermal oxidation, and recrystallization, magma resorption – in which crystal edges dissolve into ovals – is also observed. These processes leave distinct textural marks from rim to core, as a record of magmatic history.

3.2.4 Mineral Thermobarometry, Chemometry, and Magma Ascent Rate

The two-pyroxene thermobarometer (Putirka 2008) estimates crystallization pressures and temperatures using Fe-Mg exchange between orthopyroxene (Opx) and clinopyroxene (Cpx), both common in the TVG andesites. They typically form coronas (reaction rims) or contact grains. For reliable results, the Fe-Mg exchange coefficient, $K_d(\text{Fe-Mg})^{\text{Opx-Cpx}}$ should

match the theoretical value (1.09±0.14) (Putirka 2008). The method is most accurate when $Mg\#^{Cpx}$ (i.e., Mg/(Mg+Fe+Mn)) >0.75 (Putirka 2008), but for the TVG andesites, pairs with Mg# down to 0.70 are used if the K_d requirement is met. Based on Putirka's work, the two-pyroxene thermobarometric formulae yield standard errors of estimate (SEE) of T±60°C and P±280 MPa, respectively.

Amphibole-based thermobarometry estimates crystallization temperature, pressure (Ridolfi et al. 2010; Ridolfi & Renzulli 2012; Putirka 2016), and, in some cases, oxygen fugacity and H_2O content (Ridolfi & Renzulli 2012). It works for calc-alkaline magmas across wide conditions (up to 1130°C, 2.2GPa) (Ridolfi & Renzulli 2012).

Ridolfi et al. (2010) proposed a practical amphibole thermobarometer using calcic amphiboles in calc-alkaline volcanic rocks. Ridolfi and Renzulli (2012) concluded that equational errors in pressure estimates increased at higher values (P ±19.3% in avg.) and developed conditional equations calibrated for different pressure ranges to improve the accuracy of overall pressure estimates (P ±13.1% for 130-500 MPa, P ±11.4% for 930-2200MPa). On the contrary, temperature and oxygen fugacity estimates from Ridolfi and Renzulli's equations work precisely and consistently across a wide range (T ±23.5˚C for 800-1130˚C, $\log fO_2$ ±0.37). Nevertheless, Ridolfi (2021) refined the thermobarometric models up to 2200 MPa and 1130˚C, with lower errors of estimate (P ±12%, T ±22˚C, $\log fO_2$ ±0.3, H_2O in the melt ±14%); hence, Ridolfi's (2021) equations were adopted in this study. Pressure estimates are converted to crystallization depths, assuming continental crust with an average density of 2.8 g/cm^3.

Amphibole chemometric equations use calcic amphibole compositions to estimate melt major-element content (Ridolfi et al. 2010; Ridolfi & Renzulli 2012; Putirka 2016; Zhang et al. 2017). Zhang et al.'s (2017) model offers reliable predictions with consistent errors (SiO_2 at 3.78 wt.%, Al_2O_3 at 1.11 wt.%, TiO_2 at 0.16 wt.%, FeO at 1.54 wt.%, MgO at 0.64 wt.%, CaO at 1.43 wt.%, and K_2O at 0.78 wt.%).

Titanomagnetite-ilmenite pairs in equilibrium allow calculation of temperatures and oxygen fugacity using Fe-Ti oxide geothermobarometer (Carmichael 1967; Anderson 1968; Lindsley & Spencer 1982; Stromer 1983; Powell & Powell 1977; Spencer & Lindsley 1981; Anderson & Lindsley 1985), compiled by Lepage (2003) in ILMAT. Mg/Mn partitioning helps test the reliability of these results (Bacon & Hirschmann 1988).

Magma ascent rates were estimated by measuring the widths of amphibole breakdown rims (Rutherford & Devine 2003; Rutherford 2008).

3.2.5 Crystal Size Distribution (CSD)

Microcrystals were analyzed using Electron Backscattered Diffraction (EBSD) patterns collected with a JEOL JSM 5900LV SEM equipped with an Oxford-HKL Technology EBSD system (Institute of Earth Sciences, Academia Sinica, Taiwan). Patterns were obtained at 20kV, 5nA, and a 22mm working distance. Multiple EBSD images (200×180 μm) covered the groundmass, measuring over 800 feldspar microlites (1-30 μm) and micro-phenocrysts (>30 μm) per image; 5-7 images were analyzed per sample (except sample 22290: 200-300 crystals in 2 images). The EBSD system measured ellipse diameters and shape parameters for each crystal. Crystal number density (NA) was calculated as the number of whole crystals divided by the analyzed groundmass area. Only groundmass free of phenocrysts and vesicles was analyzed. Crystal size distribution (CSD) data and plots were generated using CSDCorrections software (Higgins 2000) to correct stereological artifacts.

3.2.6 Major-element Analyses

The selected samples were cut into small pieces with a diamond-bonded steel saw, then crushed to coarse sand size. After removal of visible crystals, the crushed samples were pulverized in a ball mill to obtain a fine powder. The powder was heated in two separate ovens at 110°C and 900°C to determine loss on ignition (LOI). Lithium bromide and lithium

tetraborate were added to the samples, and the mixture was fused with glass beads to produce a glass pellet. Major oxide concentrations were determined by WD-XRF using a Rigaku RIX2000 spectrometer at the Department of Geosciences, National Taiwan University. The precision of XRF analyses for major oxides (>0.5%) is estimated to be ±2%, as constrained by standard reference materials, including BHVO-2 (basalt), JGB-2 (gabbro), and GSR-1 (granite).

4. Result

4.1. $^{40}Ar/^{39}Ar$ Ages

Age spectra for the groundmass of samples DT-01_9000 and 21400 both display well-defined plateaus, giving ages of 140.4±6.1 and 474.4±10.0 ka, respectively (Tab. 1-2). In the $^{36}Ar/^{40}Ar$-$^{39}Ar/^{40}Ar$ correlation diagrams, the inverse isochrons yield 140.4±8.9 and 487.6± 20.7 ka, respectively, consistent with the plateau ages. This indicates that the plateau ages are geologically meaningful. Analytical data are detailed in Supplementary Fig. S4.

4.2. Petrography - Mineral Compositions and Texture

DT-01 samples exhibit classic porphyritic andesite texture (Fig. 4). Phenocrysts include plagioclase, clinopyroxene (augite and diopside), orthopyroxene (hypersthene), amphibole (hornblende), and titanomagnetite, with proportions detailed in Tab. 1-1.

Plagioclase phenocrysts typically show subhedral shapes and stepped or oscillatory zoning, reflecting repeated magma mixing (Fig. 4a). Some large clinopyroxenes are also zoned. Orthopyroxenes occasionally display clinopyroxene corona (Fig. 4b), indicating magma-crystal interaction. Pyroxenes often cluster as glomerophyric aggregates with magnetite inclusions (Fig. 4c). Amphibole contains diverse inclusions: plagioclase, pyroxene, and titanomagnetite. Textural relationships suggest the following mafic crystallization

sequence: titanomagnetite → orthopyroxene → clinopyroxene → amphibole.

Large, dark, oxidized amphibole phenocrysts (3-5 mm) are common throughout Lv1-Lv4, often showing poikilitic textures with granular inclusions of plagioclase, titanomagnetite, and occasionally pyroxene. Amphibole crystals exhibit strong alteration, appearing dark red or opaque. They may have opaque rims with reddish relic cores (Fig. 4d) or become fully opaque pseudomorphs (Fig. 4e). Amphibole decomposition forms polymineralic rims with varying amounts of plagioclase, pyroxene, and magnetite, depending on the governing mechanism (see Section 3.2.3).

Temporal variations in phenocryst characteristics across the Lv1-Lv4 sequence are summarized below:

In Lv1, plagioclase features oval, compositionally zoned phenocrysts (normal, reverse, and oscillatory) with high-An (occasionally high-Or) cores. Zoning records show 1-3 growth cycles from magmatic recharge. Amphibole is rare (1 vol.%, Tab. 1-1), occurring mostly as euhedral crystals with thin (ca. 15 μm) opaque rims, alongside some anhedral, resorbed varieties. Pyroxene (especially augite) oikocrysts commonly include magnetite. Millimeter-scale phaneritic enclaves (plagioclase, orthopyroxene, clinopyroxene, titanomagnetite, and, rarely, amphibole) are entrained as fragments from the shallow crust. The base of Lv1 hosts an amphibole-rich nugget (Fig. 4f) with pervasive amphibole decomposition rims, interpreted as a cumulate fragment from the reservoir.

Lv2 samples near the base are vesicle-rich. Rapid crystallization under fast growth rate is recorded by skeletal textures and cellular (spongy) cores in plagioclase (Fig. 4g), as well as skeletal or embayed pyroxene phenocrysts (Fig. 4h). Amphibole is rare except at the top of Lv2 (Tab. 1-1). Over half of the amphiboles show intense magma resorption, forming rounded or oval shapes. Amphibole appears deep red to brown, with black rims and dull interference colors (Fig. 4d), and loses high pleochroism due to microcrystalline replacement by titanomagnetite and pyroxene under oxidizing conditions. Some amphiboles are

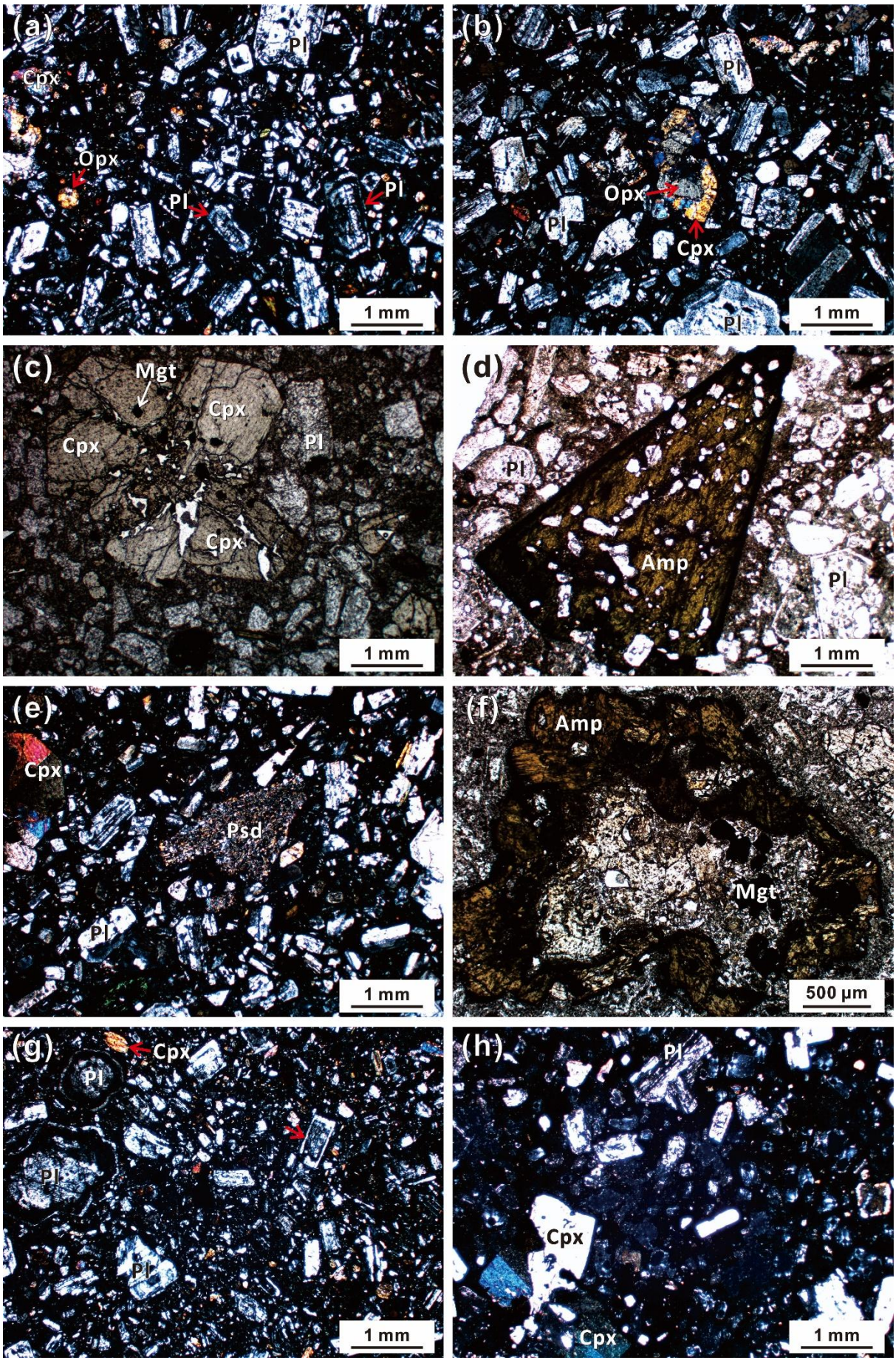
405 completely replaced by plagioclase, pyroxene, and titanomagnetite (Fig. 4e).

406 In Lv3, amphibole phenocrysts are slightly more abundant (Tab. 1-1), occurring as
407 euhedral or anhedral crystals bounded by opaque decomposition rims. In Lv4, plagioclase,
408 pyroxene, and amphibole resemble those in Lv2, but amphibole is significantly more
409 abundant (Tab. 1-1). Over half of Lv4 amphiboles have smooth, resorbed outlines, with
410 individual crystals either completely oxidized to pseudomorphs or preserving core remnants.

411 We categorized amphibole occurrences into 22 textural types in a flowchart illustrating
412 how the four mechanisms (magma decompression, thermal oxidation, recrystallization, and
413 resorption) were sequentially imposed (Fig. 5).

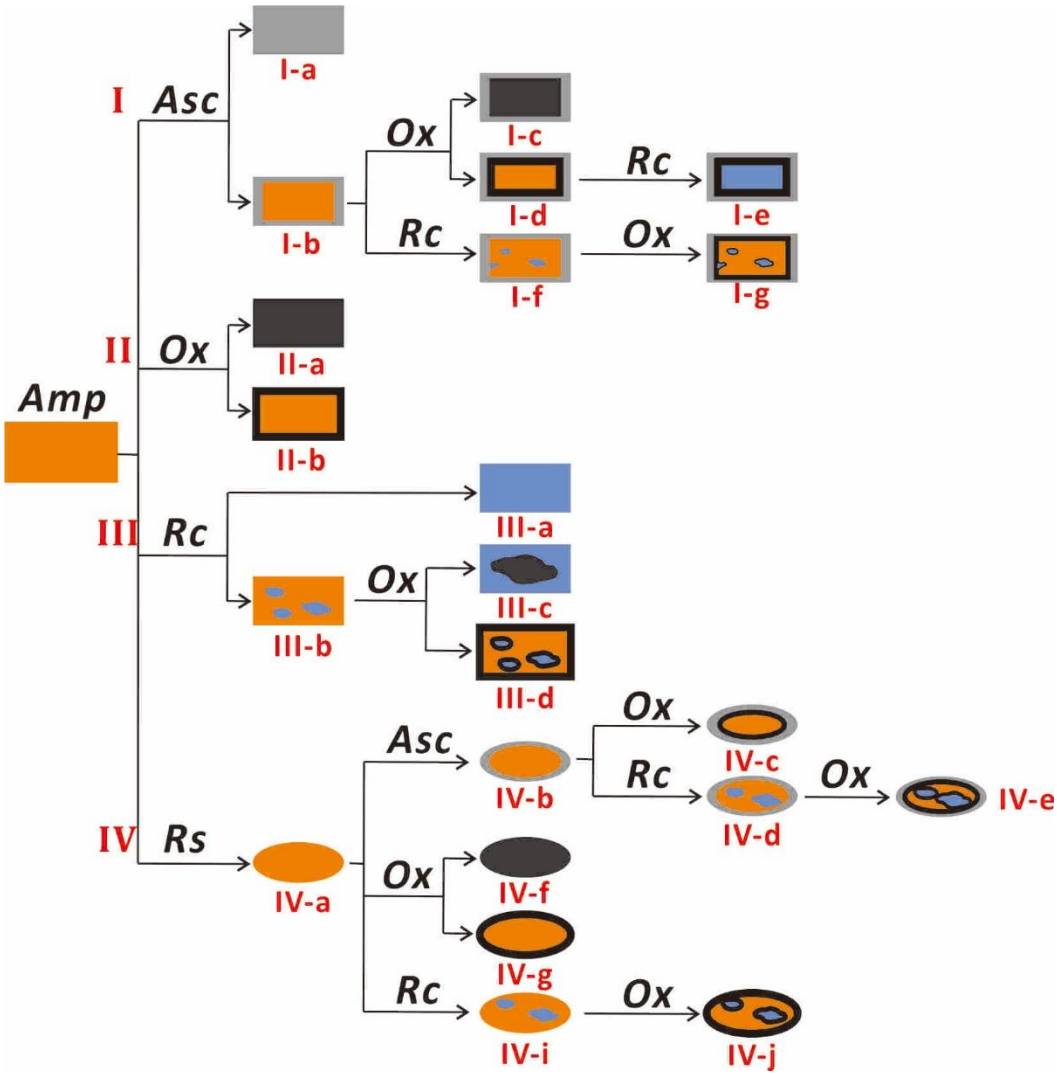
414 For example, rapidly ascending magma decompress an entrained amphibole, leading to its
415 complete replacement by pyroxene, Fe-Ti oxides, and plagioclase (I-a type; Fig. 5 & 6a) or to
416 the formation of a decompression rim (I-b type; Fig. 5 & 6b). The core of a rimmed
417 amphibole may be further replaced by thermal oxidation (I-c type; Fig. 5 & 6a), or form an
418 oxidation rim inside the decompression rim (I-d type; Fig. 5 & 6c). Thermal oxidation of
419 amphibole often creates a pseudomorph (II-a type; Fig. 5 & 6d) or an oxidation rim (II-b
420 type; Fig. 5 & 6e). Amphibole stalled in shallow magma tends to recrystallize into dehydrated
421 phases (pyroxene, plagioclase, and Fe-Ti oxides) with larger grain sizes, from the interior (III-
422 a type; Fig. 5 & 6f), sometimes growing an oxidation rim during extrusion (III-d type; Fig. 5
423 & 6g). Well-rounded, resorbed amphibole may gain a decompression rim during ascent, then
424 develop an inner oxidation rim during extrusion (IV-c type; Fig. 5 & 6h). Other amphibole
425 types are illustrated with examples in Supplementary Fig. S2.

426


(a)
Pl
Cpx
Opx
Pl
Pl
1 mm
(b)
Pl
Opx
Pl
Cpx
Pl
1 mm
(c)
Mgt
Cpx
Cpx
Pl
Cpx
1 mm
(d)
Pl
Amp
Pl
1 mm
(e)
Cpx
Psd
Pl
1 mm
(f)
Amp
Mgt
500 µm
(g)
Cpx
Pl
Pl
Pl
1 mm
(h)
Pl
Cpx
Cpx
1 mm

427

Fig. 4_Petrographic micrographs of DT-01 samples: (a) typical porphyritic texture, with phenocrysts of plagioclase (Pl), clinopyroxene (Cpx), and orthopyroxene (Opx), from sample_22930; (b) an orthopyroxene crystal developed a reaction rim (corona) of clinopyroxene, from sample_4700; (c) pyroxene crystals cluster into aggregates, forming a glomerophyric texture, from sample_16785; (d) reddish relic core of a strongly altered amphibole crystal (Amp) enclosed by an opaque rim, from sample_17300; (e) an amphibole pseudomorph (Psd) composed of a fine mixture of pyroxene, plagioclase, and titanomagnetite, from sample_17300; (f) an amphibole-rich nodule consisting of amphibole, pyroxene (center), and magnetite (Mgt), interpreted as an entrained cumulate, from sample_38270; (g) plagioclase with a skeletal texture and a cellular core (red arrow at the right), indicative of rapid crystallization, from sample_23230; (h) a skeletal-like texture in a clinopyroxene phenocryst with embayments, reflecting rapid crystal growth, from sample_20740. (a), (b), (e), (g), (h): cross-polarized light. (c), (d), (f): plane-polarized light.



441

442 Fig. 5_Flowchart of amphiboles experiencing a sequential decomposition process: I. magma
443 decompression (Asc), II. thermal oxidation (Ox), III. recrystallization (Rc), and IV. resorption
444 (Rs). Complex amphibole occurrences are summarized in the 22 textural types, from I-a to
445 IV-j, illustrating crystal evolving stages, e.g., an amphibole crystal of type I-g would undergo
446 decompression (Asc), recrystallization (Rc), and thermal oxidation (Ox) sequentially.

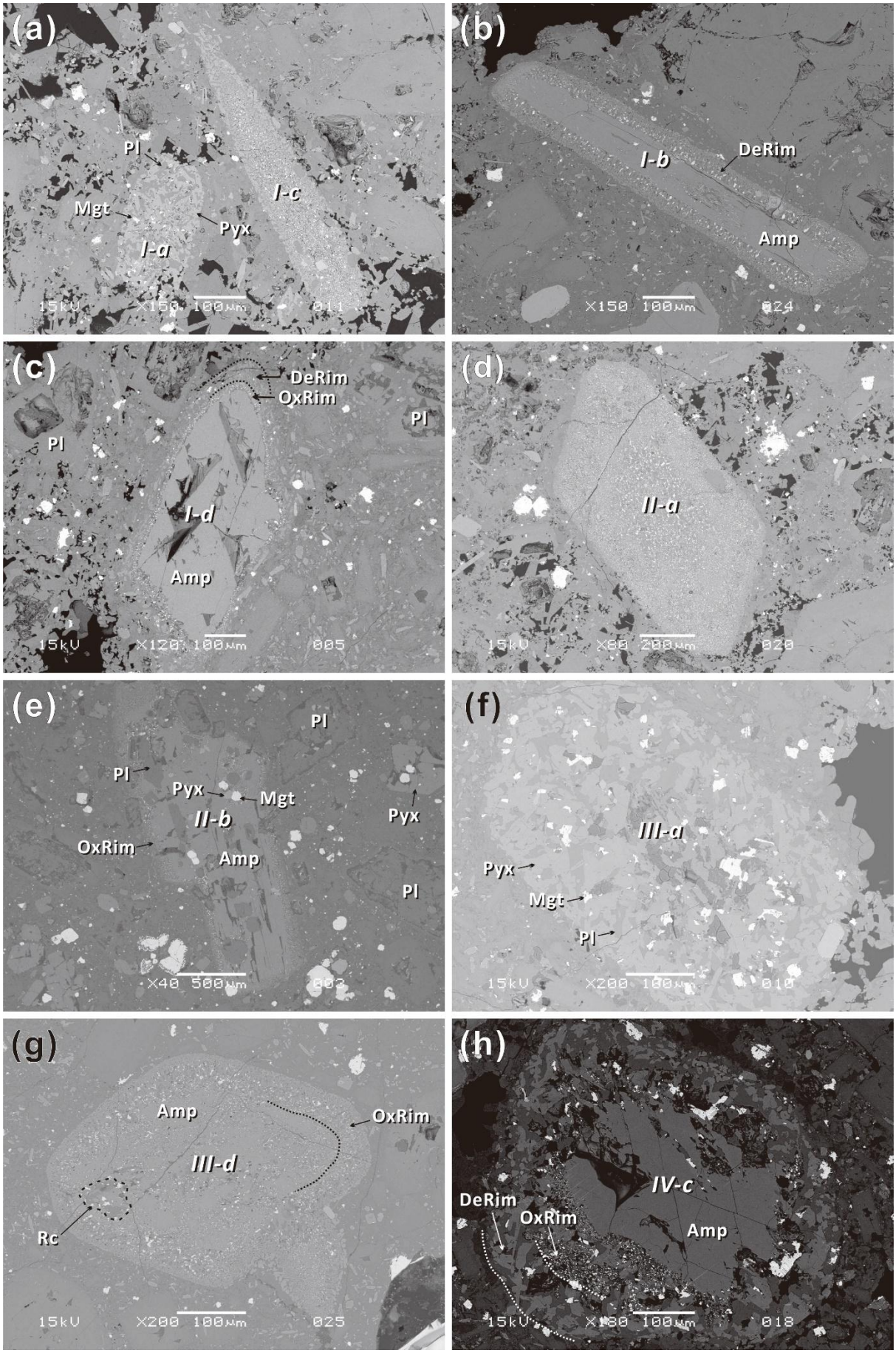


Fig. 6_Back-scattered electron images of DT-01 amphibole phenocrysts: (a) a decompressed

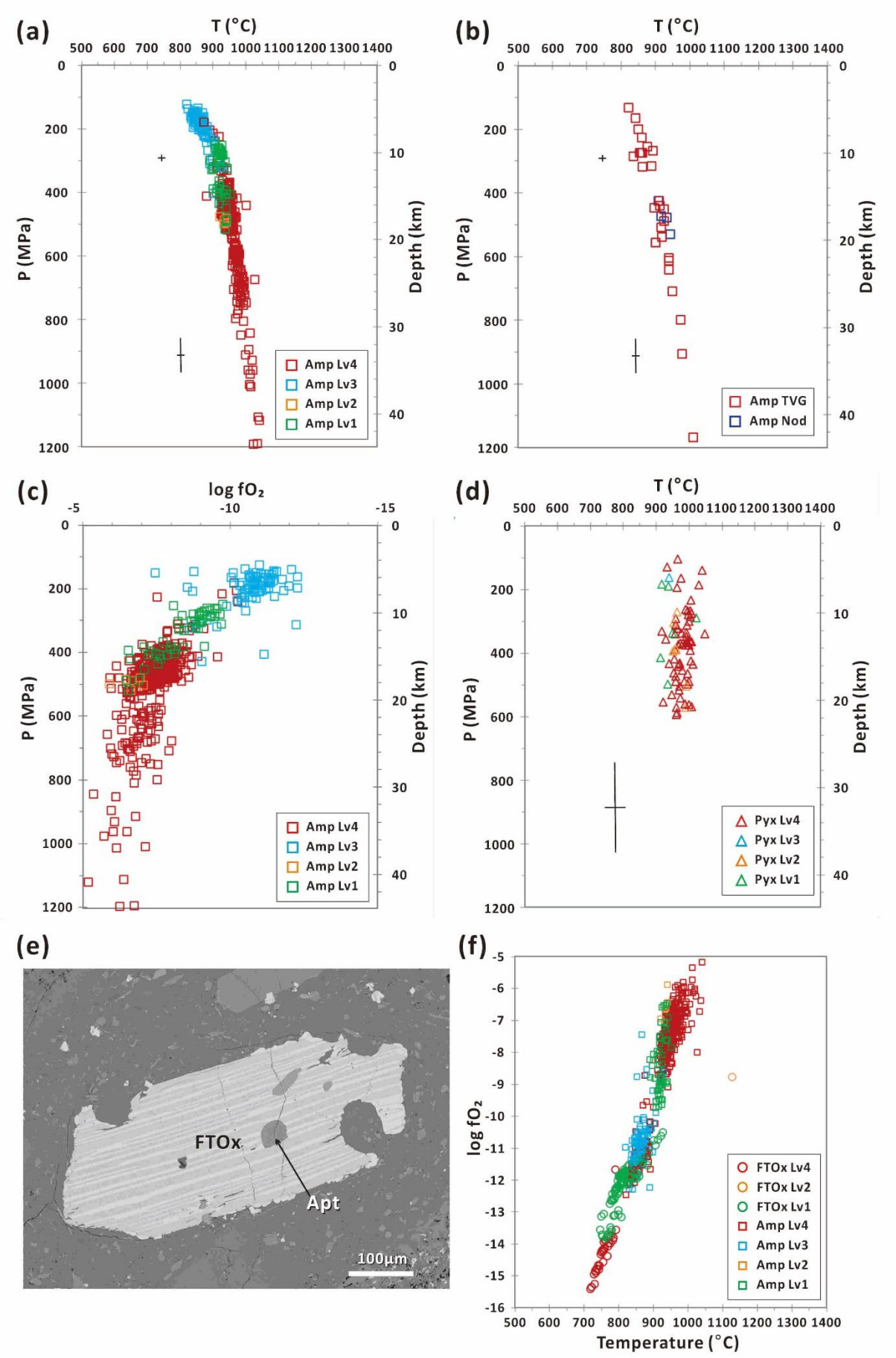
amphibole crystal (I-a type) entirely replaced by decomposition phases – pyroxene (Pyx), Fe-Ti oxides (Mgt), and plagioclase (Pl), and another (I-c type) whose interior is replaced by finer grains of decomposition phases during oxidation, from DT-01_8600; (b) an amphibole decompression rim (DeRim) (I-b type), from DT-01_17300; (c) an amphibole oxidation rim (OxRim) within the original decompression rim (I-d type), from DT-01_4700; (d) an amphibole crystal thermally oxidized to form a pseudomorph of oxidation phases (II-a type), from DT-01_8600; (e) an amphibole oxidation rim grown on the crystal edge (II-b type), from DT-01_37600; (f) amphibole recrystallization into pyroxene, plagioclase, and Fe-Ti oxides (III-a type), from DT-10_4700; (g) recrystallization patches (Rc) enclosed by an oxidation rim (III-d type), from DT-01_18600; (h) well-rounded amphibole crystals, indicative of magma-resorption, developed a decompression rim during magma ascent and then an inner oxidation rim during magma extrusion (IV-c type), from DT-10_4700. Refer to Fig. 5 for the interpretation of the amphibole occurrences.

4.3. Mineral Thermobarometric and Oxygen Fugacity Results

4.3.1. Amphibole

Amphibole thermobarometry shows crystallization conditions vary widely from Lv1 to Lv4. Lv1 amphiboles formed at 907-936 ˚C (mean 918±11 ˚C, n = 65 (9 grains)) and 247-517 MPa (mean 308±67 MPa), depths of 9-19 km (Fig. 7a). Lv2 amphiboles (rare) formed at 937 ˚C (n = 6 (1 grain)) and 524 MPa (ca. 18 km) (Fig. 7a). Lv3 amphiboles crystallized at 819-924 ˚C (mean 866±21 ˚C, n = 91 (12 grains)) and 123-426 MPa (mean 194±54 MPa), or 4-16 km (Fig. 7a). Lv4 (most abundant eruptive unit) spans 872-1041 ˚C (mean 942±34 ˚C, n = 484 (117 grains)) and 178-1191 MPa (mean 468±151 MPa), depths of 6-44 km (Fig. 7a). The data show a classic polybaric cooling trend: temperature drops by 220 °C as pressure decreases during ascent, indicating significant heat loss to the wall rock. This suggests that

475 conductive cooling dominated over latent heat from crystallization, and that ascent was
476 neither rapid nor adiabatic.
477 DT-01 amphibole thermobarometric data match amphiboles collected across the entire
478 TVG region (821-1010˚C, 133-1167 MPa; calculated from Prof. CH Chen's unpublished data,
479 Fig. 7b) and may indicate their representativeness of TVG amphibole crystallization status.
480 Chen (1978b) described ultramafic amphibole-rich nodules − cumulates of amphibole,
481 plagioclase, and magnetite − from four localities in the TVG, crystallized from parental basalt
482 magma. Their thermobarometry yields 909-942˚C and 424-531 MPa (16-19 km), offering
483 insight into the cooling TVG parental magma.
484 Oxygen fugacity from amphibole shows a reducing trend during ascent (Fig. 7c). As
485 magma ascended, the system became more reduced, with Lv3 samples most reduced
486 (oxidation states -10 to -12, near 200 MPa) and Lv4 more oxidized (cluster at oxidation states
487 -6 to -9 and 400-500 MPa). These trends record magma evolution and crystallization at
488 different crustal levels. Data are detailed in Supplementary Table S3.


(a)
T (°C)
500 600 700 800 900 1000 1100 1200 1300 1400
P (MPa)
Depth (km)
Amp Lv4
Amp Lv3
Amp Lv2
Amp Lv1
(b)
T (°C)
Amp TVG
Amp Nod
(c)
log fO2
-5 -10 -15
Amp Lv4
Amp Lv3
Amp Lv2
Amp Lv1
(d)
T (°C)
Pyx Lv4
Pyx Lv3
Pyx Lv2
Pyx Lv1
(e)
FTOx
Apt
100μm
(f)
log fO2
Temperature (°C)
FTOx Lv4
FTOx Lv2
FTOx Lv1
Amp Lv4
Amp Lv3
Amp Lv2
Amp Lv1

489

Fig. 7_DT-01 temperature, pressure (depth), and log fO_2 estimates from amphibole, 2-pyroxene, and Fe-Ti oxides: (a) amphibole data from Lv1 (green squares), Lv2 (orange squares), Lv3 (blue squares), and Lv4 (red squares). Black cross lines represent the standard error of the estimates (SEE); (b) igneous amphibole sampled across the entire TVG region (unpublished data of Prof. CH Chen, NTU, Taiwan), along with amphibole-rich nodules (blue squares); (c) amphibole pressure versus oxygen fugacity expressed as log fO_2; (d) 2-pyroxene data from Lv1 (green triangles), Lv2 (orange triangles), Lv3 (blue triangles), and Lv4 (red triangles); (e) titanomagnetite grains (FTOx) in DT-01 samples underwent thermal oxidation, forming parallel exsolution strips of ilmenite (gray) and magnetite (white); (f) the Fe-Ti oxides forming thermal exsolution at temperatures ranging from 720°C to 920°C, with lower oxygen fugacity than that of amphibole (Amp). Apt: apatite.

4.3.2. Orthopyroxene-clinopyroxene Pair (2-pyroxene)

Thermobarometric results include three pyroxene types: contact grains (orthopyroxene/clinopyroxene phenocrysts), corona (orthopyroxene with clinopyroxene rim) (Fig. 4b), and amphibole-decomposed pairs (gabbroic-type rims: Fig. 6a,b,c,h; recrystallization: Fig. 6f,g). Contact grains and coronas formed under similar conditions and exhibit a strong latent-heat signature. Overall, the pyroxenes record pressures from 100 MPa to 600 MPa at nearly constant temperatures (900–1050°C; Fig. 7d). The vertical trend indicates that latent heat from crystallization reaches balance with conductive cooling, suggesting rapid ascent.

Pyroxene contact grains and coronas depict a barometric boundary at 600 MPa (ca. 22 km; Fig. 7d), marking the onset of clinopyroxene formation. Earlier orthopyroxene likely formed at pressures similar to or higher than those at which amphibole formed, though pyroxene-melt barometry is unavailable. Pyroxene crystals record consistent temperatures (900-1050°C), unlike amphibole's cooling trend. This suggests that the amphiboles may be

antecrysts from discrete magma batches, distinct from primary-melt pyroxene, except for part of Lv4 amphiboles from the deep crust.

Amphibole-decomposed pyroxene pairs (from decompression and recrystallization) yield very low pressures (<10 MPa; Fig. 8a,b), corresponding to depths of hundreds of meters, yet retain high temperatures (900-1200°C; Fig. 8c,d). Although these pressures are beyond the empirical range of pyroxene barometry, the data indicate that amphibole decomposition occurred near the surface. Amphibole-decomposed pyroxene pairs in decompression rims (Lv1-Lv4) indicate similar temperature ranges (Fig. 8c), with 950-1020°C overlap; However, Lv1 is about 30-50°C lower than the others (Fig. 8c). Amphibole recrystallization temperatures are systematically lower than those of decompression rims and increase from Lv1 to Lv4 (Fig. 8d), suggesting decompression rims formed before recrystallization in the shallow crust. Full pyroxene thermobarometric data are in Supplementary Table S4.

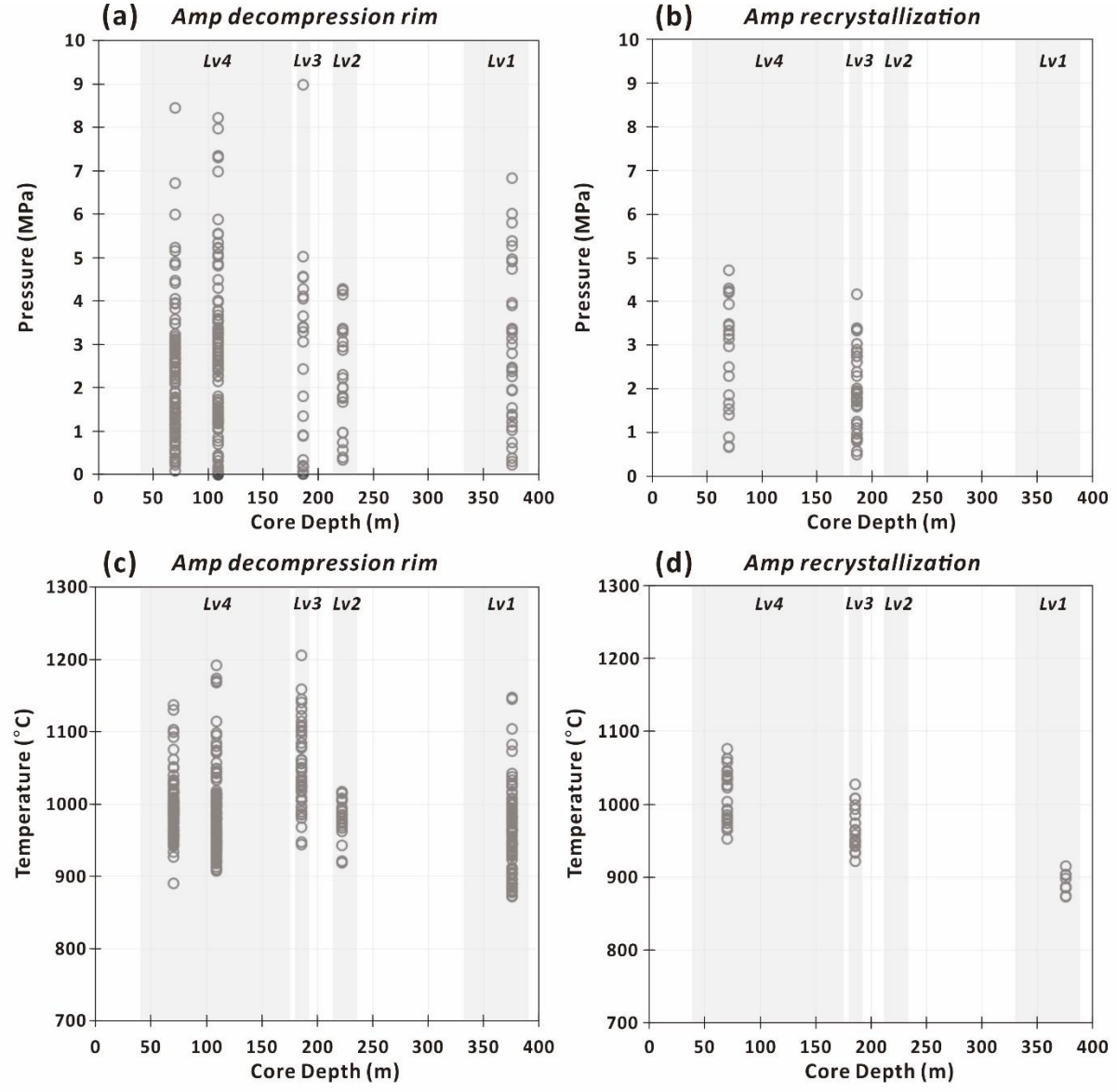


Fig. 8_Temperature and pressure conditions of amphibole decomposition phases (2-pyroxene) from thermal oxidation and recrystallization: (a) amphibole decompression rims formed at extremely low pressures, < 10 MPa (within hundreds of meters depth); (b) amphibole recrystallization occurred at depths almost as shallow as the decompression rims; (c) amphibole decompression rims retain high temperatures between 900-1200°C; (d) amphibole recrystallization temperatures are systematically lower than those of amphibole decompression rims, which show an elevation trend from Lv1 to Lv4. Pressure estimates below 0 are neglected in (a) and (b).

4.3.3. Fe-Ti Oxides Pair

Fe-Ti oxides (magnetite-group) ideally form ilmenite/magnetite couples for thermometry, but such equilibrium pairs are rare in DT-01 samples. Instead, titanomagnetite grains often show thermal oxidation, producing alternating ilmenite/magnetite exsolution strips (matrix: low-Ti magnetite; lamellae: ilmenite) (Fig. 7e). These strips record lower temperatures (720-920°C) and oxygen fugacity (-10 ~ -15) than amphibole (Fig. 7f). Titanomagnetite exsolution likely relates to amphibole thermal oxidation, reducing the magmatic redox state. The Fe-Ti oxide pairs examined by Mg/Mn partitioning are mostly located near the equilibrium line, within the volcanic separates field (Supplementary Fig. S3).

4.4. Magma Ascent Rate

Magma ascent rates from amphibole rims in DT-01 samples are 0.004-0.011 m/s, aligning with those documented in extrusive eruptions at volcanoes such as St. Helens, Soufriere Hills, and Black Butte (Rutherford 2008, Tab. 2). Within the DT-01 core section, Lv1 samples exhibit the highest ascent rates (0.011 m/s). Lv2 samples lack measurable rims, while Lv3 and Lv4 samples show lower rates (0.004-0.008 m/s). Explosive eruptions worldwide have magma ascent rates at least 10-100 times higher than the estimates in DT-01 (Tab. 2). Hence, DT-01 samples reflect effusive activities from gentle eruptions.

Tab. 2_Magma ascent rates estimated from amphibole decompression rims in DT-01 samples. Data for other volcanoes (St. Helens, Soufriere Hills, Unzen, and Black Butte) are from Rutherford 2008.

Volcano	Observation Tool	Explosive Ascent rate (m/s)	Extrusive Ascent Rate (m/s)
St. Helens, US	Groundmass crystallization	>> 0.2	0.01 – 0.02
St. Helens, US	Amphibole rim	> 0.018	0.004 – 0.015
Soufriere Hills, Mont.	Amphibole rim	> 0.2	0.001 – 0.012

Soufriere Hills, Mont.	Magnetite	> 0.2	0.003 – 0.015
Unzen JP	Magnetite zonation	Not present	0.002
Black Butte CA	Amphibole rim	Not present	0.004 – 0.006
DT-01 core, TVG			
Lv 1	Amphibole rim	Not present	0.011
Lv 3	Amphibole rim	Not present	0.004 – 0.008
Lv 4	Amphibole rim	Not present	0.004 – 0.006

561

562 **4.5. Crystallization Size Distribution (CSD)**

563 Crystal size distributions (CSDs) of feldspar microlites (excluding Lv3 for lack of
564 microlites) from DT-01 samples display similar upward-deflecting curves (Fig. 9), with steep
565 slopes for small crystals and gentler slopes for larger ones − patterns typical of crystal
566 accumulation (Marsh 1988), in contrast to a downward-deflecting curve implying crystal
567 fractionation (Marsh, 1988). Lv4 samples (Fig. 9a,b), with the slowest ascent rate (Tab. 2),
568 exhibit larger crystal size (ca. 0.6 mm) and stronger crystal growth (e.g., Preece et al. 2013)
569 than Lv1 and Lv2 samples (Fig. 9c,d). Some Lv4 samples (Fig. 9a) show higher y-axis
570 intercepts (ca. 20 mm^{-4}), indicating that nucleation dominates during rapid cooling (e.g.,
571 Preece et al. 2013), whereas Lv2's lower intercept (ca. 16 mm^{-4}) (Fig. 9c) suggests greater
572 undercooling and shorter crystallization times.

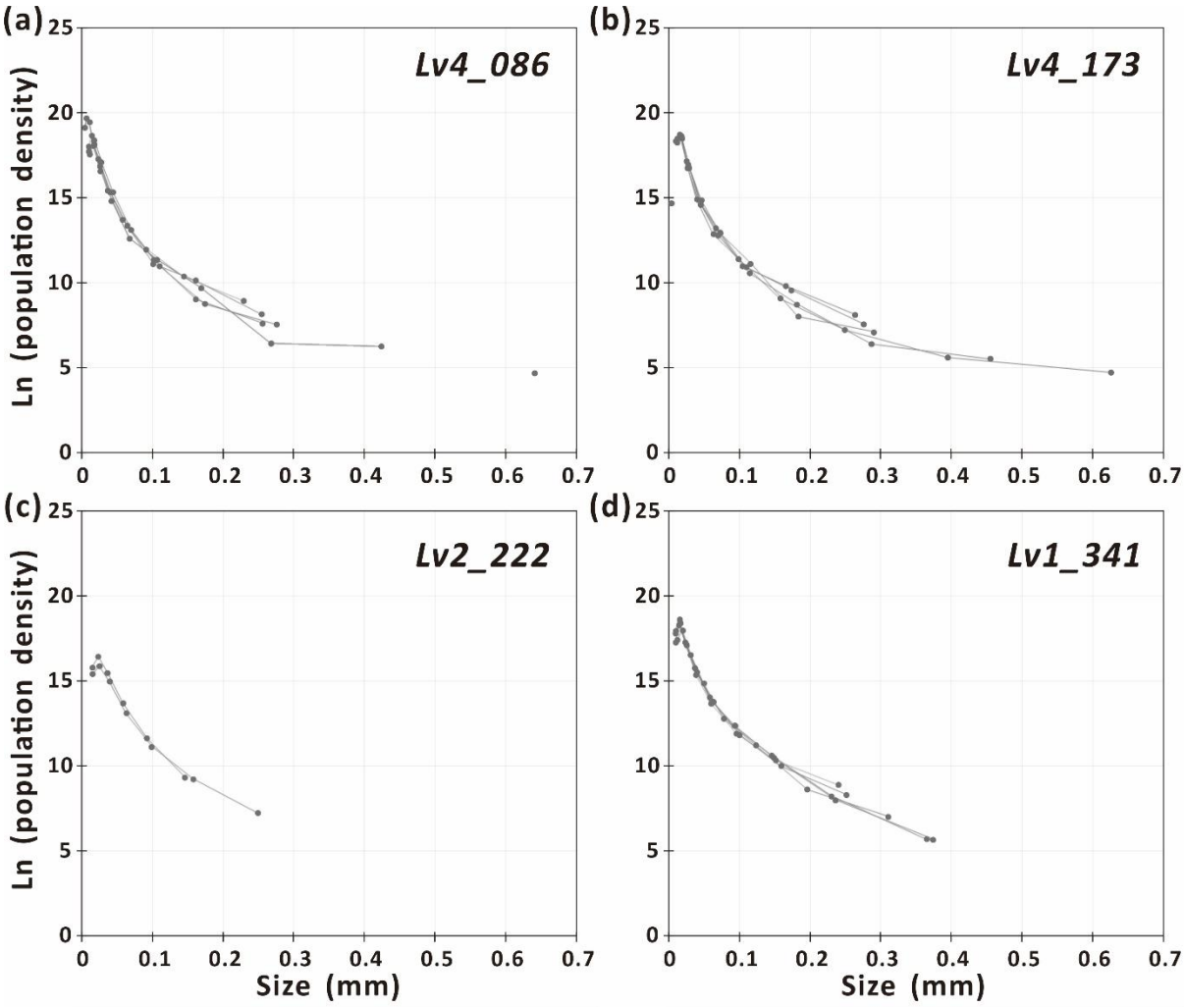


Fig. 9_Crystal size distributions (CSDs) illustrating feldspar microlite nucleation and growth in DT-01 samples. (a) The Lv4 sample, with the slowest magma ascent rate, exhibits an upward-concave curve indicating strong crystal growth. Its high y-axis intercept (nearly 20 mm^{-4}) indicates nucleation dominance under rapid cooling. (b) Some Lv4 samples reach larger crystal sizes above 0.6 mm. (c) The Lv2 sample illustrates a lower y-axis intercept (about 16 mm^{-4}) and smaller crystal size, resulting from melt undercooling in a short crystallization time. (d) The Lv1 sample, similar to Lv4, exhibits a slightly upward-concave line for crystal growth. Samples in Lv3 have no CSD data for the glassy groundmass lacking microlites.

4.6. Bulk Rock Chemistry - Major-element Compositions

TVG volcanic rocks plot as basaltic andesite to andesite (Song et al. 2004, 2006, 2008) in the total alkalis versus silica (TAS) diagram (Fig. 10a), with DT-01 samples identified as basaltic andesite, matching earlier studies. Major-element data for DT-01 samples are given in Supplementary Table S1. In the K_2O versus SiO_2 diagram (Fig. 10b), TVG volcanic rocks are mainly medium-K calc-alkaline, with a small portion of high-K samples (Song et al. 2011); DT-01 samples also show high-K and medium-K calc-alkaline trends. Amphibole-based melt estimates for DT-01 samples show 51.5-76.6% silica (andesite or rhyolite), 0.1-2.7% MgO (2.6-5.4% for the TVG volcanic rocks), and 0.1-9.4% CaO (6.4-9.5% for the TVG volcanic rocks) (Supplementary Table S2).

Amphibole-equilibrated melt compositions from Lv1-Lv4 illustrate magma compositional evolution. Lv1-Lv2 are high- and medium-K calc-alkaline andesite (58-67% silica) (Fig. 10b), while Lv3 shifts to medium-K calc-alkaline dacite (62-74% silica) (Fig. 10b). This compositional variation suggests progressive crystal fractionation. Lv4 displays polarized compositions (Fig. 10b) − medium-K calc-alkaline basaltic andesite (55-62% silica) or dacite (67-74% silica) − revealing a significant blending event of mafic and acidic host magmas.

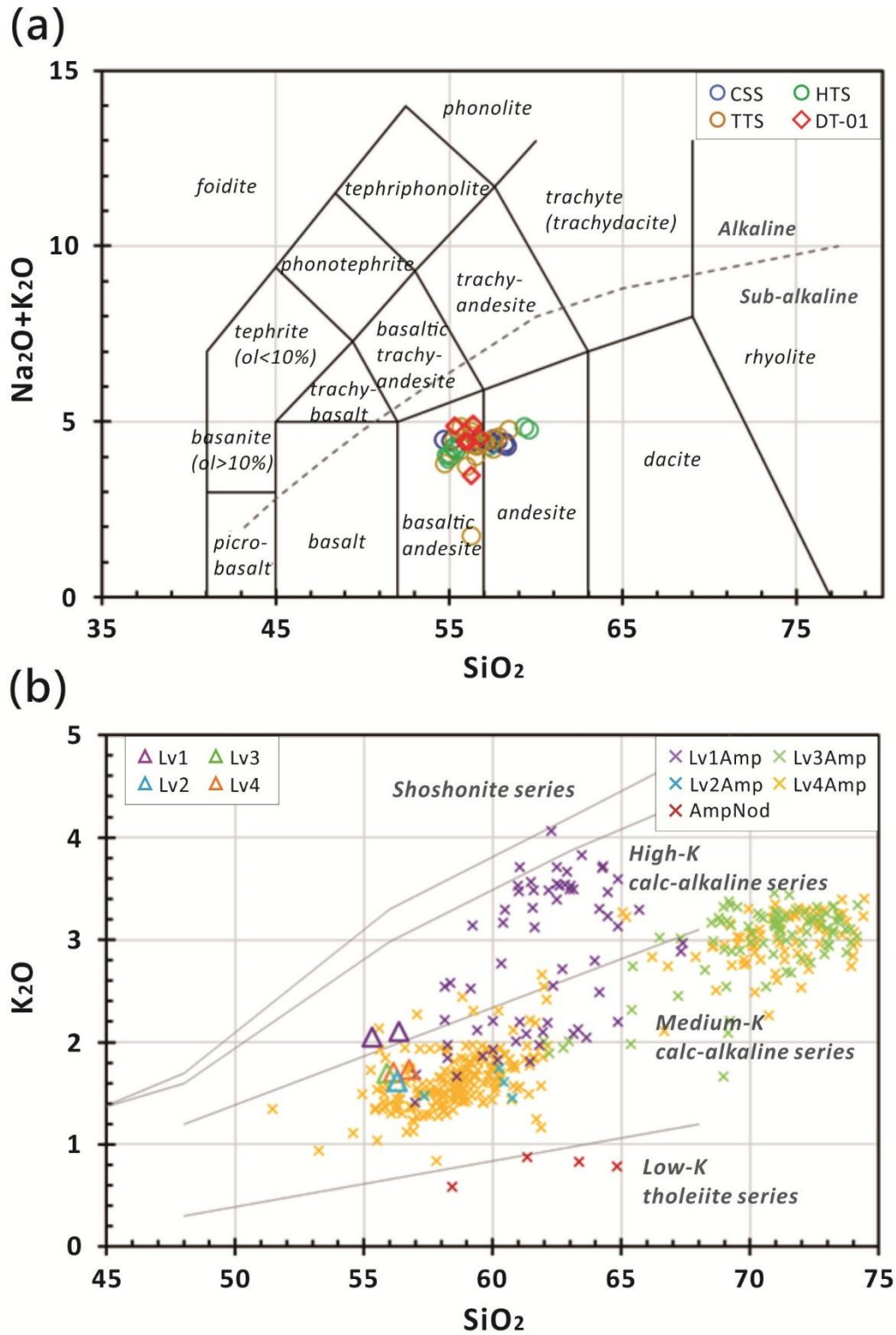


Fig. 10_(a) Total alkalis-silica (TAS) diagram of the TVG volcanic rocks − Chihsing volcanoes (CSS), Huangtsui volcanoes (HTS), Tatun volcanoes (TTS) (Song et al. 2004, 2006, 2007), and the DT-01 core (this study). (b) K_2O vs SiO_2 plots. Cross symbols − Lv1, Lv2, Lv3, Lv4, and AmpNod − represent melt compositions estimated from amphiboles in Lv1, Lv2, Lv3, Lv4, and amphibole-rich nodules, respectively, using amphibole chemometric

equations (Zhang et al. 2017). Whole-rock compositions of Lv1, Lv2, Lv3, and Lv4 are presented with triangle symbols.

5. Discussion

5.1. Mineral Constraints on Magma Crystallization Process

TVG magma crystallization, based on DT-01 petrography and mineral thermobarometry, began with orthopyroxene formation in primary magmas, initiating magma fractionation and a compositional shift from basaltic to basaltic andesitic. As magma intruded into the crust and cooled below 1050°C, amphibole crystallized in stagnant magma batches. When parental magma ascended to pressures around 600 MPa (ca. 22 km depth), clinopyroxene formed, releasing latent heat and maintaining temperatures at 950-1000 °C. Meanwhile, crustal magma batches containing amphibole were trapped by magma mixing as the replenished magmas rose, explaining amphibole's cooling trend with decreasing depth. Phenocryst growth halts at 100 MPa (ca. 4 km), representing a stagnation ceiling for magma. Above this depth, rapid eruptive ascent led to decompression rims on amphiboles under shallow-crustal conditions, as indicated by pyroxene thermobarometry. The amphibole-derived pyroxenes, forming at temperatures above 900°C, align with the groundmass, which shows typical high-temperature crystal nucleation and accumulation patterns in CSD plots.

Some titanomagnetite grains exhibit textures of exsolution lamellae indicative of weak thermal oxidation (Yang & Chen 1994). Ilmenite-magnetite geothermometry (Carmichael 1967; Anderson 1968; Lindsley & Spencer 1982; Stromer 1983; Lepage 2003) reveals that thermal exsolution occurred at subsolidus temperatures (780-870°C) (Supplementary Table S5), reflecting the cold lock-up state of a highly crystallized magma prior to eruption.

5.2. Magma Evolution

DT-01 samples disclose that amphibole crystals experienced decompression, thermal

633 oxidation, recrystallization, and resorption at different stages, resulting in overprinted textures
634 such as crystal decomposition, corona, and rounding. These features reflect amphibole
635 evolution in relation to dominant magmatic processes (Shane & Smith 2013; Erdmann et al.
636 2014; Nagasaki et al. 2017).

637 Amphibole crystal from the same depth locality developed distinct textural occurrences
638 (Fig. 5), which may imply numerous interconnected chambers scattered throughout the crust
639 along magma ascent pathways, acting as crustal buffers for amphibole crystallization (Fig.
640 11). Inside these chambers, fractionated intermediate magmas—derived from primary mafic
641 magmas—incrementally rose and cooled, promoting amphibole growth (Fig. 11). During
642 magma ascent, processes such as crystal fractionation (with orthopyroxene, amphibole, and
643 clinopyroxene crystallizing sequentially), magma stagnation (ca. 4-22 km depths, favoring
644 amphibole growth), and mixing (recharged mafic magmas and fractionalized magma batches)
645 occurred. Mineral evidence (phenocryst growth) places the shallow reservoir ceiling at ca. 4
646 km (Fig. 7). The amphibole decompression rim suggests a much shallower depth than 4 km
647 (Supplementary Table S4). Further amphibole decomposition from thermal oxidation and
648 recrystallization occurred near the surface, as indicated by amphibole features and pyroxene
649 barometric data (Fig. 5, Fig. 11, Supplementary Table S4).

650 Magma extrusion from Lv1 to Lv4 was steady at a nearly consistent rate (0.004-0.011
651 m/s; Tab. 2) across a lengthy period over 0.33 million years (Tab. 1-2). This effusive eruption
652 style aligns with the magmatism of an extensional tectonic setting (Wang et al. 2004), rather
653 than subduction (Juang & Bellon 1984; Juang 1993; Teng 1996). Post-collisional rifting in
654 northern Taiwan caused asthenosphere upwelling (for crustal thinning; Wang et al. 2004) and
655 low crustal stress, enabling gentle, steady magma release through the crustal rifting system
656 (branches of Shanchiao fault; Fig. 2). This resulted in predominantly low-explosivity, effusive
657 eruptions in the TVG, as supported by field and genetic topographic studies (Chang et al.
658 2006; Chen et al. 2003, 2007).

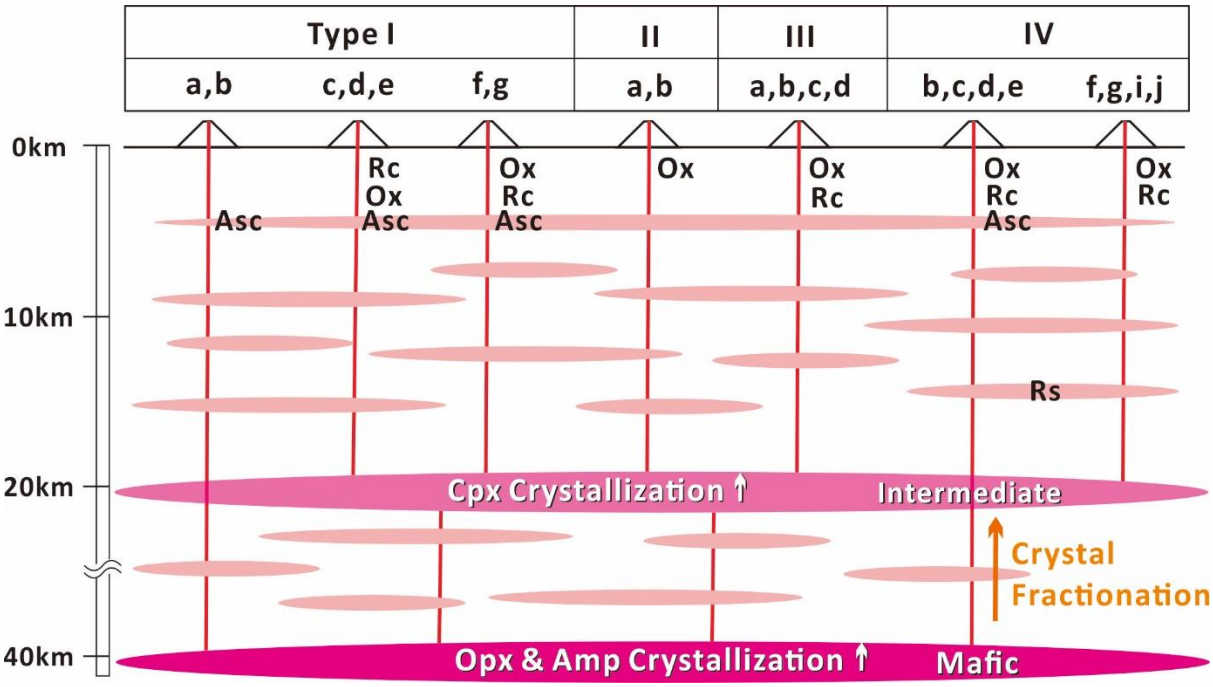


Fig. 11_Illustration of amphibole evolution routes based on amphibole decomposition processes (Fig. 5) and mineral thermobarometry. Numerous magma batches dispersed throughout the crust act as buffers for amphibole crystallization. These fractionated intermediate magma batches, derived from primary mafic magmas, gradually cooled during ascent and produced abundant amphiboles. As the primary magma ascended, it underwent crystal fractionation (orthopyroxene, amphibole, and clinopyroxene), magma segregation (favoring amphibole crystallization), magma stagnation (at depths of 4-22 km), and magma mixing (recharged mafic magmas and fractionated magma batches), sequentially.

5.3. Magma Genesis of the Tatun Volcano Group

Crystal constraints reveal that TVG primary magmas originated from mantle depths exceeding 40 km, deeper than the Moho (ca. 35 km in northern Taiwan: Ma et al. 1996; Lin 2016). The geochemical model (Wang et al. 2004) suggests TVG magmas formed by partial melting of upwelling asthenospheric mantle (ca. 2.6 Ma). Seismic study (Lin et al., 2021) found delayed P-wave scatterings at 60-95 km depths beneath northern Taiwan, linked to mantle-wedge diapirs from the subducted slab, supporting a connection between TVG magma

676 formation and the subducted Philippine Sea Plate.

677 Pressure and temperature variations recorded by TVG crystals depict magma migration
678 from the asthenospheric mantle to the shallow crust, accompanied by crystal fractionation and
679 magma differentiation. An amphibole-rich inclusion in our sample (Fig. 4f) aligns with
680 amphibole-rich nodules described by Chen (1978, 1980), consisting of unzoned amphibole,
681 plagioclase, and magnetite of similar composition. They are interpreted as cumulates from
682 parental mafic magma, supporting the magma fractionation assumption in which a high-
683 alumina basaltic magma transforms into andesitic magma through the removal of these
684 nodules (Chen 1978b, 1980). The nodule amphiboles yield 909-942 ˚C and 16-19 km at depth
685 using amphibole compositions of Chen (1978b) (Fig. 7b), and their parental magma falls
686 within the low-K tholeiite series (Fig. 10), similar to the parental magmas of the offshore
687 islets in northeastern NTVZ (Wang et al. 2000, 2004). These findings signify that amphibole-
688 rich nodule accumulation within the TVG magma reservoir drives magma differentiation.

689 Amphibole cumulates play a unique role in arc magmatism, acting as cryptic
690 fractionation (Smith 2013) or water filters for mantle-derived magmas (Davison et al. 2007).
691 Amphibole can fractionate cryptically through reactions between melts and mush in the lower
692 crustal reservoir, producing amphibole-rich assemblages without forming visible amphibole
693 phenocrysts, as evidenced by the similar REE signature between clinopyroxene relics and
694 amphibole replacements (Smith 2014). In such cases, evolved melts overprint earlier
695 clinopyroxene, creating granoblastic amphibole lithologies at the expense of the earlier
696 clinopyroxene. However, TVG amphibole-rich nodule textures lack typical features of
697 clinopyroxene-derived amphibole, such as amphibole blebs within clinopyroxene, poikilitic
698 amphibole replacing clinopyroxene, or amphibole rims around clinopyroxene nodules, as
699 described by Smith (2014). Instead, it is more plausible that amphibole crystals simply sank
700 to the bottom of the TVG main magma reservoir (ca. 20 km), forming amphibole-rich
701 nodules. Disseminated chambers at varied crustal depths (above the main reservoir) also

produced amphiboles, driving localized magma fractionation toward andesitic-dacitic compositions, as evidenced by the wide temperature and pressure range of entrained amphiboles.

5.4. Magma Reservoir Models

Numerous studies have used multidisciplinary approaches – geochemistry, petrology, seismology, geodesy, and magnetotellurics–to investigate volcanic plumbing systems (Andronico et al. 2005; Dahren et al. 2012; Field et al. 2012; Harangi et al. 2015; Jay et al. 2014; Kahl et al. 2011; Peccerillo et al. 2006; Piochi et al. 2009; Viccaro et al. 2016; Widiyantoro et al. 2018; Nurfiani et al. 2021). These studies revealed magma storage zones and eruptible volumes, supporting the interpretation of monitoring data for pre-eruptive signals. Nonetheless, they focused on active volcanoes with recent eruptions to analyze current plumbing systems.

We define late Pleistocene magma reservoir conditions (the petrologic model) using mineral thermobarometry and petrology to compare with the present-day reservoir estimated from seismic wave modeling (Lin et al. 2025) and 3-D tomographic joint inversion (Huang et al. 2021; Lin et al. 2024), referred to as the seismological model. Differences in timing and dimensions among the two reservoir models suggest temporal and spatial variations within the reservoir, implying a long-term trend toward future eruptibility. Our petrologic model places magma stagnation depths (based on crystallization levels) between 4-40 km (Fig. 12). Most magmas are supposed to contain >50% crystals in a lock-up status (Cooper & Kent 2014). Amphiboles that crystallized from the melt partly sank to the reservoir's bottom at ca. 20 km, as inferred from the ultrabasic nodules' amphibole (Chen 1978). The seismological model shows a reservoir at depths of 8-20 km beneath northeastern Taiwan, with an average melt fraction of 19.2% (Huang et al. 2021) and an eruptible zone (>50% melt fraction) below 14 km (Lin et al. 2025) (Fig. 12). Given uncertainties in the petrologic model's volume

estimate, the upper limit of phenocryst crystallization depth, ca. 4 km, may represent the late Pleistocene reservoir ceiling, whereas the current reservoir ceiling lies at depths of 8 km according to the seismological model. The retreat of the reservoir ceiling from the late Pleistocene to the present indicates a substantial reduction in the reservoir's volume.

In active volcanoes, variations in crystallization depth across an eruptive sequence usually indicate magma migration patterns in the lithosphere (Putirka 1996, 1997, 2008, 2017). However, the four DT-01 lava units, spanning long periods — exceeding 0.33 million years (Tab. 1-2) — each represent distinct eruptive epochs. Differences in stagnation depth between these units may reflect dynamic adjustments of the reservoir and conduit space due to magma replenishment, partial eruptions, and stimulation of cold crustal magma bodies (Blundy et al. 2006; Cooper 2017), rather than magma migration trends.

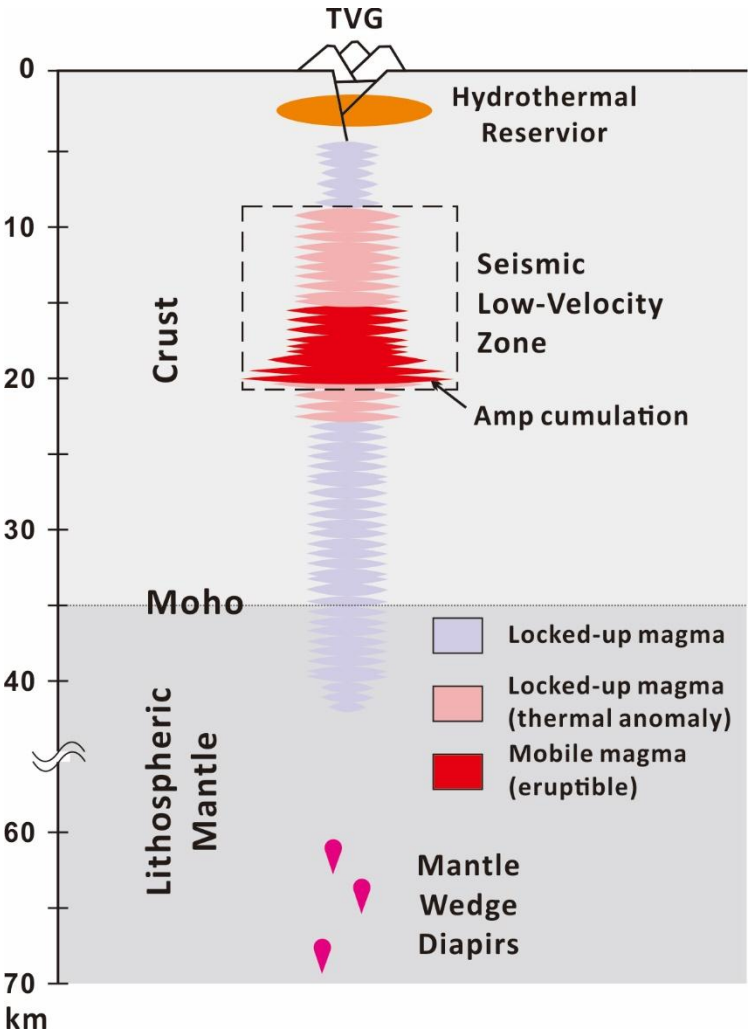


Fig. 12_ Conceptual model of the TVG magma reservoir, compiled from Huang et al. (2021), Lin et al. (2025), and this study. Magma stagnation depths, constrained by crystals, ranged from 40 to 4 km and were mostly stored in a locked-up state with high crystallinity. Based on estimates from amphibole-rich nodules (Chen 1978), part of the amphibole crystals sank to the bottom of the main reservoir at ca. 20 km depth. The main magma reservoir beneath northeastern Taiwan, at depths of 8-20 km, retains more melt (>50% by fraction) below 14 km, interpreted as an eruptible portion. The upper limit of the crystallization depth at 4 km corresponds to the ceiling of the late Pleistocene magma reservoir, whereas seismology estimates the present reservoir ceiling at 8 km.

5.5. Eruption Potential of the Tatun Volcano Group

Wang et al. (2004) proposed that NTVZ magmatism is driven by two geodynamic mechanisms: (1) asthenospheric upwelling from post-collisional extension of the northern Taiwan mountain belt during the Pliocene-Pleistocene, and (2) melting of upwelling asthenospheric mantle influenced by the Ryukyu subduction system (Fig. 1). Accordingly, we evaluate TVG's long-term eruptibility considering NTVZ tectonic conditions linked to the aforementioned mechanisms during the Pleistocene and at present.

1. Seismic tomography locates the TVG magma reservoir at 8-20 km depths beneath northeastern Taiwan (Huang et al. 2021). Detecting a large liquid magma body suggests the potential of imminent eruptions (Cooper & Kent 2014). P-wave scattering obstacles at 60-95 km depths (Fig. 12) imply the presence of mantle wedge diapirs sourced from the subducted slab (Lin et al. 2021), supporting the generation of slab-dehydration fluid beneath the Ryukyu subduction system.
2. Paleostress data from northern Taiwan indicate E-W compression in the Pliocene (Lu et al. 1995; Hu et al. 2002), which shifted to post-collision extension in the Pleistocene, enabling TVG magmatism. During the Pleistocene, northern Taiwan's

extensional stress field caused crustal thinning and asthenospheric upwelling, triggering partial melting (Wang et al. 2004). Present-day stress field data from earthquake focal mechanisms (Yeh et al. 1991; Hsu et al. 2009), stress tensor inversion (Hsu et al. 2009), and GPS strain-rate field (Hu et al. 2002; Hsu et al. 2009) reveal that northern Taiwan lies within a transitional regime (neither contraction nor extension) (Fig. 1), with tectonic stability and minimal strain (Hu et al. 2002; Hsu et al. 2009; Pu et al. 2020), suggesting that crustal thinning and asthenospheric upwelling have ceased.

While mantle wedge diapirs from the subducted Philippine Sea Plate still contribute slab-dehydration fluid, crustal thinning-induced partial melting in the overriding Eurasian Plate has probably ceased, given the stable stress state and very low strain rate in northern Taiwan. As a result, magma accumulation in the reservoir should be slower at present, prolonging eruption recurrence intervals or retarding reservoir pressure buildup, and eventually easing eruptive potential. It also leads to low magma ascent rates and limited effusive activities, as observed by Chen et al. (2003, 2007) and Belousov et al. (2010).

A major hydrothermal reservoir at depths of 2-4 km beneath the TVG is well documented (Fig. 12) (Komori et al. 2014; Huang et al. 2017; Lin et al. 2019; Pu et al. 2020; Lin et al. 2024) and may serve as a shallow magma chamber, priming an imminent eruption, in which amphibole antecryst decomposition initiated (Fig. 11). Therefore, fresh magma intruding into the shallow hydrothermal reservoir should be a serious concern. It is highly recommended to monitor anomalous variations in the hydrothermal reservoir as a precursor to an upcoming eruption.

6. Concluding Remarks

In the late Pleistocene, TVG magma stagnated at depths between 4- 40 km in a locked-up state. Ascent involved sequential crystal fractionation, magma stagnation, and

792 mixing, modifying the magma composition from mafic to intermediate and ending with
793 crystal accumulation during eruptive cooling.
794 TVG plumbing system consisted of multiple crustal chambers during the Pleistocene.
795 Amphibole-rich nodules from primitive melts depict the main reservoir floor at ca. 20 km
796 depth, while petrologic data place the late Pleistocene reservoir ceiling at 4 km. The present-
797 day seismological data reveal that the reservoir ceiling has retreated to 8 km (with an 8-20 km
798 storage depth). The retreat indicates a significant reduction in reservoir volume.
799 Steady, long-term effusive extrusion (0.004-0.011 m/s for >0.33 Myr) supports an
800 extensional tectonic setting driven by post-collisional rifting in northern Taiwan, rather than
801 active subduction. However, the present tectonic stability in the northern Taiwan region
802 suggests that magma from asthenospheric upwelling has ceased. The diminished magma
803 supply consequently implies longer recurrence intervals of volcanic unrest, thereby reducing
804 eruptive potential. Future eruptions may be primed by a hydrothermal reservoir at 2-4 km
805 beneath the TVG (where amphibole antecryst decomposition initiated); fresh magma
806 intrusion into this zone should be an imminent eruption precursor to monitor**.**

Acknowledgement

This research was supported by the Taiwan Volcanic Activity Monitoring Project, funded by the Geological Survey and Mining Management Agency, MOEA, Taiwan (114-1406-02-28-04). We thank Ms. Masako Usuki, Mr. Fu-Long Lin, and Mr. Guang-Sheng Yeh for their assistance during the experiments. We also appreciate the valuable discussions and feedback from Prof. Wei-Teh Jiang and Prof. Huai-Jen Yang of National Cheng Kung University.

Supplementary Information

Additional file 1. Supplementary Information. (ESM_1.docx)

Additional file 2. Supplementary Material. (ESM_2.xlsx)

Author Contributions

GTH: Conceptualization, Methodology, Investigation, Formal Analysis, Data Curation, Writing-Original Draft, Writing-Review & Editing. KLW: Methodology, Review & Editing, Supervision. YI: Formal Analysis, Data Curation, Review & Editing. CHC: Methodology, Data Curation, Review & Editing. YSW: Formal Analysis, CSD Data Curation. CHL: Review & Editing. YHL: Ar-Ar Data Curation. DPM: Ar-Ar Data Curation. All authors read and approved the final manuscript.

Declarations

Competing Interests

The authors declare no competing interests.

Data Availability

All data supporting the findings of this study are available within the paper and its Supplementary Information files. Any datasets used in this study but not included above are also available from the corresponding author on reasonable request.

Research Funding Statements:

This study is supported by the Geological Survey and Mining Management Agency, MOEA, Taiwan [the Taiwan volcanic activity monitoring project: 114-1406-02-28-04] and partially supported by National Science and Technology Council (NSTC) of Taiwan (114-2116-M-001-013-: YI). The content is solely the responsibility of the authors and does not necessarily represent the official views of the Geological Survey and Mining Management Agency.

References

Anderson AT (1968) Oxidation of the La Blanche Lake titaniferous magnetite deposit, Québec. J Geol 76(4):528-547.

Anderson DJ, Lindsley DH (1985) New (and final!) models for the Ti-magnetite/ilmenite geothermometer and oxygen barometer. Abstract AGU 1985 Spring Meeting Eos Transactions. AGU 66(18):416.

Andronico D, Branca S, Calvari S, Burton M, Caltabiano T, Corsaro RA, Del Carlo P, Garfi G, Lodato L, Miraglia L, Murè F, Neri M, Pecora E, Pompilio M, Salerno G, Spampinato L (2005) A multi-disciplinary study of the 2002-03 Etna eruption: insights into a complex plumbing system. Bull Volcanol 67:314-330.

Bacon CR, Hirschmann MM (1988) Mg/Mn partitioning as a test for equilibrium between coexisting Fe-Ti oxides. Am Mineral 73:57-61.

Belousov A, Belousov M, Chen C-H, Zellmer GF (2010) Deposits, character and timing of recent eruptions and gravitational collapses in Tatun Volcanic Group, northern Taiwan: hazard-related issues. J Volcanol Geotherm Res 191:205-221.

857 Blundy J, Cashman K (2005) Rapid decompression-driven crystallization recorded by melt
858 inclusions from Mount St. Helens volcano. Geology 33:793-796.
859 Blundy J, Cashman K, Humphreys M (2006) Magma heating by decompression-driven
860 crystallization beneath andesite volcanoes. Nature 443:76-80.
861 Browne B (2005) Petrologic and experimental constraints on magma mingling and ascent:
862 examples from Japan and Alaska. PhD thesis. University of Alaska, Fairbanks.
863 Browne BL, Gardner JE (2006) The influence of magma ascent path on the texture,
864 mineralogy, and formation of hornblende reaction rim. Earth Planet Sci Lett 246(3-
865 4):161-176.
866 Carmichael ISE (1967) The iron-titanium oxides of salic volcanic rocks and their associated
867 ferromagnesian silicates. Contrib Min Petrol 14(1):36-64.
868 Chan YC, Lee JC, Liu CC, Hu JC, Chen WS, Chen RF, Cheng DY, Hsu WC (2005)
869 Investigation and monitoring of special geological hazards in the greater Taipei area –
870 High-precision airborne LiDAR topographic mapping and tectonic geomorphic analysis
871 (1/3). Report of Central Geological Survey, MOEA, Taiwan (in Chinese with English
872 abstract).
873 Chen CH (1975) Petrological and chemical study of volcanic rocks from Tatun volcano
874 group. Proc Geol Soc China 18:59-72.
875 Chen CH (1978a) Petrochemistry and origin of Pleistocene volcanic rocks from northern
876 Taiwan. Bull Volcanol 41(4):513-528.
877 Chen CH (1978b) Significance of ultramafic inclusions in Tatun Volcano Group, northern
878 Taiwan. Proc Geol Soc China 21:80-91.
879 Chen CH, Lin SB (2000) Distribution and significance of volcanic materials in sediments of
880 the Taipei Basin. J Geol Soc China 43(2):287-310.
881 Chen CH, Lin SB (2002) Eruptions younger than 20 Ka of the Tatun Volcano Group as
882 viewed from the sediments of the Sungshan Formation in Taipei Basin. West Pac Earth

883 Sci 2(2):193-206.
884 Chen CH, Burr GS, Lin SB (2010) Time of a near Holocene volcanic eruption in the Tatun
885 Volcano Group, northern Taiwan: evidence from AMS radiocarbon dating of charcoal
886 ash from sediments of the Sungshan Formation in Taipei Basin. Terr Atmos Ocean Sci
887 21(3):611-614.
888 Chen CH, Wu YJ (1971) Volcanic geology of the Tatun geothermal area, northern Taiwan.
889 Proc Geol Soc China 14:5-20.
890 Chen WS, Yang CC, Yang HC, Liu JK (2003) Volcanic landform and sequences of the Tatun
891 volcanoes. Bull Central Geol Surv 16:99-123. (in Chinese with English abstract)
892 Chen WS, Yang CC, Yang HC, Liu JK, Chan YC, Shea KS, Hsieh YC (2007) Scanning Laser
893 Mapping (2Mx2M DTM) of the Pleistocene Tatun Volcanic Landform. Bull Central
894 Geol Surv 20:101-128. (in Chinese with English abstract)
895 Chu MF, Lai YM, Li Q, Chen WS, Song SR, Lee HY, Lin TH (2018) Magmatic pulses of the
896 Tatun Volcano Group, northern Taiwan, revisited: Constraints from zircon U-Pb ages and
897 Hf isotopes. J Asian Earth Sci 167:209-217. https://doi.org/10.1016/j.jseaes.2018.05.028
898 Cooper KM (2017) What Does a Magma Reservoir Look Like? The “Crystal's-Eye” View
899 Elements 13(1):23-28.
900 Cooper KM, Kent AJR (2014) Rapid remobilization of magmatic crystals kept in cold
901 storage. Nature 506:480-483. DOI: 10.1038/nature12991
902 Crosweller HS, Arora B, Brown SK, Cottrell E, Deligne NI, Guerrero NO, Hobbs L,
903 Kiyosugi K, Loughlin SC, Lowndes J, Nayembil M, Siebert L, Sparks RSJ, Takarada S,
904 Venzke E (2012) Global database on large magnitude explosive volcanic eruptions
905 (LaMEVE). J Applied Volc 1:4. DOI:10.1186/2191-5040-1-4.
906 Dahren B, Troll VR, Andersson UB, Chadwick JP, Gardner MF, Jaxybulatov K, Koulakov I
907 (2012) Magma plumbing beneath Anak Krakatau volcano, Indonesia: evidence for
908 multiple magma storage regions. Contrib Mineral Petrol 163:631-651. DOI

10.1007/s00410-011-0690-8

Davison J, Turner S, Handley H, Macpherson C, Dosseto A (2007) Amphibole “sponge” in arc crust? Geology 35(9):787-790. Doi: 10.1130/G23637A.1

DeAngelis SHD, Larsen J, Coombs M (2013) Pre-eruptive magmatic conditions at Augustine Volcano, Alaska, 2006: Evidence from amphibole geochemistry and textures. J Petrol 54(9):1939-1961. Doi:10.1093/petrology/egt037

DeAngelis SHD, Larsen J, Coombs M, Dunn A, Hayden L (2015) Amphibole reaction rims as a record of pre-eruptive magmatic heating: An experimental approach. Earth Planet Sci Lett 426:235-245. http://dx.doi.org/10.1016/j.epsl.2015.06.051

Devine JD, Rutherford MJ, Gardner JE (1998) Petrologic determination of ascent rates for the 1995-1997 Soufriere Hills Volcano andesitic magma. Geophys Res Lett 25(19):3673-3676. DOI: 10.1029/98GL00912

Devine JD, Rutherford MJ, Norton GE, Young SR (2003) Magma storage region processes inferred from geochemistry of Fe-Ti oxides in andesitic magma, Soufriere Hills Volcano, Montserrat, WI. J Petrol 44:1375-1400.

Erdmann S, Martel C, Pichavant M, Kushnir A (2014) Amphibole as an archivist of magmatic crystallization conditions: problems, potential, and implications for inferring magma storage prior to the paroxysmal 2020 eruption of Mount Merapi, Indonesia. Contrib Mineral Petrol 167:1016. DOI 10.1007/s00410-014-1016-4

Field L, Blundy J, Brooker RA, Wright T, Yirgu G (2012) Magma storage conditions beneath Dabbahu Volcano (Ethiopia) constrained by petrology, seismicity and satellite geodesy. Bull Volcanol 74:981-1004. DOI 10.1007/s00445-012-0580-6

Garcia MO, Jacobson SS (1979) Crystal clots, amphibole fractionation and the evolution of calc-alkaline magmas. Contrib Min Petrol 69:319-327.

Geschwind CH, Rutherford MJ (1995) Crystallization of microlites during magma ascent: the fluid mechanics of 1980-86 eruptions at Mount St. Helens. Bull Volcanol 57:356-370.

Harangi S, Kiss ANB, Seghedi I, Lukács R, Szarka L, Wesztergom V, Metwaly M, Gribovszki K (2015) Combined magnetotelluric and petrologic constrains for the nature of the magma storage system beneath the Late Pleistocene Ciomadul volcano (SE Carpathians). J Volcanol Geotherm Res 290:82-96. http://dx.doi.org/10.1016/j.jvolgeores.2014.12.006

Higgins MD (2000) Measurement of crystal size distributions. Am Mineral 85:1105-1116.

Holland TJB, Blundy JD (1994) Non-ideal interactions in calcic amphiboles and their bearing on the amphibole-plagioclase thermometry. Contrib Mineral Petrol 116:433-447.

Hong GT (2014) Characteristics of the pyroclastic rocks from Chutzeshan volcano subgroup, northern Taiwan in relation to volcanic eruption styles. Bull Central Geol Surv 27:1-25. (in Chinese with English abstract)

Hsu YJ, Yu SB, Simmons M, Kuo LC, Chen HY (2009) Interseismic crustal deformation in the Taiwan plate boundary zone revealed by GPS observations, seismicity, and earthquake focal mechanisms. Tectonophys 479:4-18. DOI: 10.1016/j.tecto.2008.11.016

Hu JC, Yu SB, Chu HT, Angelier J (2002) Transition tectonics of northern Taiwan induced by convergence and trench retreat. Geol Soc Am Spec Pap 358:149-162.

Huang YC, Lin CH, Kagiyama T (2017) Shallow crustal velocities and volcanism suggested from ambient noise studies using a dense broadband seismic network in the Tatun Volcano Group of Taiwan. J Volcanol Geotherm Res 341:6-20. http://dx.doi.org/10.1016/j.volgeores.2017.05.016

Huang HH, Wu ES, Lin CH, Ko JYT, Shih MH, Koulakov I (2021) Unveiling Tatun volcanic plumbing structure induced by post-collisional extension of Taiwan mountain belt. Sci Rep 11:5286.

Ignacio LARC, Lee YH, Jabagat KD, Iizuka Y, Lin CH, Hong GT (2026) Magma Storage and Eruptive History of the Mt. Qixing, Tatun Volcano Group, Taiwan: Insights from Petrology and Thermobarometry [Conference presentation abstract]. AOGS 2026 23rd

961 annual meeting, Fukuoka, Japan.
962 Jabagat KD, Lee YH, Danišík M, Miggins D, Chu MF, Lai YM, Lo YC, Lee PT, Lin CH
963 (2026) Late quaternary eruption history of the Tatun Volcano Group (Taiwan) – new
964 constraints from zircon double-dating and $^{40}Ar/^{39}Ar$ dating of lava flows in Mt. Shamao.
965 Tectonophysics 924(2026)231083. https://doi.org/10.1016/j.tecto.2026.231083
966 Jay J, Costa F, Pritchard M, Lara L, Singer B, Herrin J (2014) Locating magma reservoirs
967 using InSAR and petrology before and during the 2011-2012 Cordón Caulle silicic
968 eruption. Earth Planet Sci Lett 395:254-266. https://doi.org/10.1016/j.epsl.2014.03.046
969 Johnson MC, Rutherford MJ (1989) Experimental calibration of the aluminum-in-hornblende
970 geobarometer with application to Long Valley caldera (California) volcanic rocks.
971 Geology 17:837-841.
972 Juang WS (1993) Diversity and origin of Quaternary basaltic magma series in northern
973 Taiwan. Bull Natl Mus Nat Sci 4:125-166.
974 Juang WS, Bellon H (1984) The potassium-argon dating of andesites from Taiwan. Proc Geol
975 Soc China 27:86-100.
976 Juang WS, Chen JC (1989) Geochronology and geochemistry of volcanic rocks in northern
977 Taiwan. Bull Central Geol Surv 5:31-66.
978 Kahl M, Chakraborty S, Costa F, Pompilio M (2011) Dynamic plumbing system beneath
979 volcanoes revealed by kinetic modeling, and the connection to monitoring data: An
980 example from Mt. Etna. Earth Planet Sci Lett 308(1-2):11-22.
981 https://doi.org/10.1016/j.epsl.2011.05.008
982 Koppers AAP, Staudigel H, Wijbrans JR (2000) Dating crystalline groundmass separates of
983 altered Cretaceous seamount basalts by the $^{40}Ar/^{39}Ar$ incremental heating technique.
984 Chem Geol 166:139-158.
985 Koppers AAP (2002) ArArCALC-Software for $^{40}Ar/^{39}Ar$ age calculations. Comput Geosci
986 28:605-619.

Kear D (1957) Erosional stages of volcanic cones as indicators of age. New Zealand J Sci Technol 38:671-682.

Klügel A, Hansteen TH, Schminke H-U (1997) Rates of magma ascent and depths of magma reservoirs beneath La Palma (Canary Island). Terranova 9:117-121.

Klügel A, Klein F (2005) Complex storage and ascent at embryonic submarine volcanoes from the Madeira Archipelago. Geology 34:337-340.

Komori S, Utsugi M, Kagiyama T, Inoue H, Chen CH, Chiang HT, Chao BF, Yoshimura R, Kanda W (2014) Hydrothermal system in the Tatun Volcano Group, northern Taiwan, inferred from crustal resistivity structure by audio-magnetotellurics. Prog Earth Planet Sci 1:20.

Kong F, Lawver LA, Lee TY (2000) Evolution of the southern Taiwan-Sinzi Folded Zone and opening of the southern Okinawa trough. J Asian Earth Sci 18:325-341.

Lee SF (1996) The study of the Chihsingshan Volcano Subgroup lava sequence in Tatun Volcano Group. Master thesis, Natl Taiwan Univ (NDLTD in Taiwan. https://hdl.handle.net/11296/7ax55v)

Lee YH, Miggins DP, Marcaida M, Jabagat K (2023) The Ar-Ar and U-Th/He disequilibrium dating ages of Tatun volcano group and neighboring volcanoes. Proceedings of the 2023 Annual Meeting of the Chinese Geophysical Society and the Geological Society of China.

Lee YH, Miggins DP, Marcaida M, Danisik M, Jabagat K, Lai YM, Tang HY, Chu MF (2024) The recent eruptive ages of Shamao volcano: 15,000 or 1370 yr. Proceedings of the 2024 Annual Meeting of the Chinese Geophysical Society and the Geological Society of China.

Ignacio LARC, Lee YH, Jabagat KD, Iizuka Y, Lin CH, Hong GT (2026) Magma Storage and Eruptive History of the Mt. Qixing, Tatun Volcano Group, Taiwan: Insights from Petrology and Thermobarometry. [Conference presentation abstract] AOGS 23rd Annual

1013 Meeting, Sg.
1014 Lepage LD (2003) ILMAT: an Excel worksheet for ilmenite-magnetite geothermometry and
1015 geobarometry. Comput Geosci 29:673-678.
1016 Liao CK (2018) The study of young explosive craters in the Chihsingshan area, Tatun
1017 volcano group. Master thesis, Natl Taiwan Univ (in Chinese with English abstract)
1018 http://tdr.lib.ntu.edu.tw/jspui/handle/123456789/69995
1019 Lin CH (2016) Evidence for a magma reservoir beneath the Taipei metropolis of Taiwan from
1020 both S-wave shadows and P-wave delays. Sci Rep 6:39500; doi: 10.1038/srep39500
1021 Lin CH, Lai YC, Shih MH, Lin CJ, Ku JS, Huang YC (2019) A major hydrothermal reservoir
1022 underneath the Tatun Volcano Group of Taiwan: Clues from a dense linear geophone
1023 array. Pure Appl Geophys 177:2889-2902. https://doi.org/10.1007/s00024-019-02396-w
1024 Lin CH, Shih MH, Lai YC (2021) Mantle wedge diapirs detected by a dense seismic array in
1025 Northern Taiwan. Sci Rep 11:1561. https://doi.org/10.1038/s41598-021-81357-7
1026 Lin CH, Lai YC, Shih MH (2025) Strong seismic reflections indicating possible eruptible
1027 magma beneath the Tatun Volcano Group in Taiwan. Sci Rep 15:24333
1028 https://doi.org/10.1038/s41598-025-09558-y
1029 Lin YP, Ko JYT, Huang BS, Lin CH, Shih MH (2024) Unveiling attenuation structures in the
1030 northern Taiwan volcanic zone. Sci Rep 14:4716 http://doi.org/10.1038/s41598-024-
1031 55397-8
1032 Lindsley DH, Spencer KJ (1982) Fe-Ti oxide geothermometry: Reducing analyses of
1033 coexisting Ti-magnetite (Mt) and ilmenite (Ilm) abstract AGU 1982 Spring Meeting Eos
1034 Transactions. AGU 63(18):471.
1035 Lu CY, Angelier J, Chu HT, Lee JC (1995) Contractional, transcurrent, rational and
1036 extensional tectonics: Examples from Northern Taiwan. Tectonophys 125:129-146.

1037 Lucchi F (2019) On the use of unconformities in volcanic stratigraphy and mapping: Insights
1038 from the Aeolian Islands (southern Italy). J Volcanol Geotherm Res 385:3-26.
1039 https://doi.org/10.1016/j.volgeores.2019.01.014
1040 Ma KF, Wang JH, Zhao D (1996) Three-dimensional seismic velocity structure of the crust
1041 and uppermost mantle beneath Taiwan. J Phys Earth 44:85-105.
1042 Marsh BD (1988) Crystal size distribution (CSD) in rocks and the kinetics and dynamics of
1043 crystallization. I. Theory. Contrib Min Petrol 99:277-291.
1044 Martí J, Groppelli G, Silveira AB (2018) Volcanic stratigraphy: A review. J Volcanol
1045 Geotherm Res 357:68-91. https://doi.org/10.1016/j.volgeores.2018.04.006
1046 McCanta MC, Rutherford MJ, Hammer JE (2007) Pre-eruptive and syn-eruptive conditions in
1047 the Black Butte, California dacite: Insight into crystallization kinetics in a silicic magma
1048 system. J Volcanol Geotherm Res 160:263-284.
1049 Murphy MD, Sparks RSJ, Barclay J, Carroll MR, Brewer TS (2000) Remobilization of
1050 andesite by intrusion of mafic magma at the Soufrière Hills Volcano, Montserrat, West
1051 Indies. J Petrol 41(1):22-42.
1052 Nagasaki S, Ishibashi H, Suwa Y, Yasuda A, Hokanishi N, Ohkura T, Takemura K (2017)
1053 Magma reservoir conditions beneath Tsurumi volcano, SW Japan: Evidence from
1054 amphibole thermobarometry and seismicity. Lithos 278-281:153-165.
1055 Nakamura M (1995) Continuous mixing of crystal mush and replenished magma in the
1056 ongoing Unzen eruption. Geology 23:807-810.
1057 Nurfiani D, Wang X, Gunawan H, Triastuty H, Hidayat D, Wei SJ, Taisne B, Bouvet de
1058 Maisonneuve C (2021) Combining petrology and seismology to unravel the plumbing
1059 system of a typical arc volcano: An example from Marapi, West Sumatra, Indonesia.
1060 Geochem Geophys Geosyst 22:e2020GC009524.
1061 https://doi.org/10.1029/2020GC009524

1062 Piochi M, De Astis G, Petrelli M, Ventura G, Sulpizio R, Zanetti A (2009) Constraining the
1063 recent plumbing system of Vulcano (Aeolian Arc, Italy) by textural, petrological, and
1064 fractal analysis: The 1739 AD Pietre Cotte lava flow. Geochem Geophys Geosyst
1065 10(1):1-28. https://doi.org/10.1029/2008gc002176
1066 Powell R, Powell M (1977) Geothermometry and oxygen barometry using coexisting iron-
1067 titanium oxides: a reappraisal. Mineral Mag 41(318):257-263.
1068 Preece K, Barclay J, Gertisser R, Herd RA (2013) Textural and micro-petrological variations
1069 in the ruptive products of the 2006 dome-forming eruption of Merapi volcano,
1070 Indonesia: Implications for sub-surface processes. J Volcanol Geotherm Res 261:98-120.
1071 http://dx.doi.org/10.1016/j.jvolgeores.2013.02.006
1072 Pu HC, Lin CH, Lai YC, Shih MH, Chang LC, Lee HF, Lee PT, Hong GT, Li YH, Chang
1073 WY, Lo CH (2020) Active volcanism revealed from a seismicity conduit in the long-
1074 resting Tatun Volcano Group of northern Taiwan. Sci Rep 10:6153.
1075 https://doi.org/10.1038/s41598-020-63270-7
1076 Putirka K, Johnson M, Kinzler R, Walker D (1996) Thermobarometry of mafic igneous rocks
1077 based on clinopyroxene-liquid equilibria, 0-30 kbar. Contrib Mineral Petrol 123:92-108.
1078 Putirka K (1997) Magma transport at Hawaii: inferences from igneous thermobarometry.
1079 Geology 25:69-72.
1080 Putirka KD, Condit C (2003) A cross section of a magma conduit system at the margins of the
1081 Colorado Plateau. Geology 31:701-704.
1082 Putirka KD (2008) Thermometers and barometers for volcanic systems. Rev Mineral
1083 Geochem 69:61-120.
1084 Putirka K (2016) Amphibole thermometers and barometers for igneous systems and some
1085 implications for eruption mechanisms of felsic magmas at arc volcanoes. Am Mineral
1086 101:841-858.

1087 Putirka KD (2017) Down the crater : Where magmas are stored and why they erup. Elements
1088 13:11-16. doi:10.2113/gselements.13.1.11
1089 Ridolfi F. (2021) Amp-TB2: An updated model for calcic amphibole thermobarometry.
1090 Minerals 11:324.
1091 Ridolfi F, Puerini M, Renzulli A, Menna M, Toukeridis T (2008) The magmatic feeding
1092 system of El Reventador volcano (Sub-Andean zone, Ecuador) constrained by texture,
1093 mineralogy and thermobarometry of the 2002 erupted products. J Volcanol Geotherm
1094 Res 176:94-106.
1095 Ridolfi F, Renzulli A (2012) Calcic amphiboles in calc-alkaline magmas: thermobarometric
1096 and chemometric empirical equations valid up to 1,130˚C and 2.2 Gpa. Contrib Mineral
1097 Petrol 163:877-895.
1098 Ridolfi F, Renzulli A, Puerini M (2010) Stability and chemical equilibrium of amphibole in
1099 calc-alkaline magmas: An overview, new thermobarometric formulations and application
1100 to subduction-related volcanoes. Contrib Mineral Petrol 160:45-66. doi:10.1007/s00410-
1101 009-0465-7
1102 Rutherford MJ, Hill PM (1993) Magma ascent rates from amphibole breakdown:
1103 Experiments and the 1980-1986 Mount St. Helens eruptions. J Geophys Res 98:19667-
1104 19685.
1105 Rutherford MJ, Devine JD (2003) Magmatic conditions and magma ascent as indicated by
1106 hornblende phase equilibria and reactions in the 1995-2001 Soufriere Hills magma. J
1107 Petrol 44:1433-1454.
1108 Rutherford MJ (2008) Magma Ascent Rates. Rev Mineral Geochem 69:241-271.
1109 Scaillet B, Evans BW (1999) The 15 June 1991 eruption of Mount Pinatubo. I. Phase
1110 equilibria and pre-eruption P-T-fO_2-fH_2 conditions of the dacite magmas. J Petrol
1111 40:381-411.

1112 Schmidt MW (1992) Amphibole composition in tonalite as a function of pressure; an
1113 experimental calibration of the Al-in-hornblende barometer. Contrib Mineral Petrol
1114 110:304-310.
1115 Shane P, Smith VC (2013) Using amphibole crystals to reconstruct magma storage
1116 temperatures and pressures for the post-caldera collapse volcanism at Okataina volcano.
1117 Lithos 156-159:159-170. http://dx.doi.org/10.1016/j.lithos.2012.11.008
1118 Shellnutt JG, Belousov A, Belousova M, Wang KL, Zellmer GF (2014) Generation of calc-
1119 alkaline andesite of the Tatun volcanic group (Taiwan) within an extensional
1120 environment by crystal fractionation. Int Geol Rev 56(9):1156-1171.
1121 Doi:10.1080/00206814.2014.921865
1122 Smith DJ (2014) Clinopyroxene precursors to amphibole sponge in arc crust. Nat Commum
1123 5:4329. https://doi.org/10.1038/ncomms5329
1124 Song SR, Lee YH, Lu YC, Yang YM, Liao CK, Lin JY (2017) Age dating of volcanic rocks
1125 in Tatun Volcano Group. Report of Central Geological Survey, MOEA, Taiwan (in
1126 Chinese with English abstract).
1127 Song SR, Yang FTY, Lo W (2004) Investigation and monitoring of special geological hazards
1128 in the greater Taipei area - Geological and geochemical investigation and monitoring for
1129 volcanic hazards in metropolitan Taipei (1/4). Report of Central Geological Survey,
1130 MOEA, Taiwan (in Chinese with English abstract).
1131 Song SR, Yang FTY, Lo W (2006) Investigation and monitoring of special geological hazards
1132 in the greater Taipei area - Geological and geochemical investigation and monitoring for
1133 volcanic hazards in metropolitan Taipei (3/4). Report of Central Geological Survey,
1134 MOEA, Taiwan (in Chinese with English abstract).
1135 Song SR, Yang FTY, Jiang ST, Tsai YW (2008) Investigation and monitoring of special
1136 geological hazards in Taipei area, Phase II. - Geological and geochemical investigation

and monitoring for volcanic hazards in metropolitan Taipei (1/4). Report of Central Geological Survey, MOEA, Taiwan (in Chinese with English abstract).

Song SR, Yang FTY, Jiang ST, Tsai YW (2011) Investigation and monitoring of special geological hazards in Taipei area, Phase II. 4-year final report. Central Geological Survey, MOEA (in Chinese with English abstract).

Song SR, Yang YM, Tang HY, Chiu YL (2021) The study of explosive craters along the Chihsingshan rifting valleys. Comm Res Rep Yangmingshan Natl Park (in Chinese with English abstract).

Sparks RSJ, Young SR, Barclay J, Calder ES, Cole P, Daroux B, Davies MA, Druitt TH, Harford C, Herd R, James M, Lejeune AM, Loughlin S, Norton G, Skerrit G, Stasiuk MV, Stevens NS, Toothill J, Wage G, Watts R (1998) Magma production and growth of the lava dome of the Soufriere Hills volcano, Montserrat: November 1995 to December 1997. Geophys Res Lett 25:3421-3425.

Spencer KJ, Lindsley DH (1981) A solution model for coexisting iron-titanium oxides. Am Mineral 66(11-12):1189-1201.

Stromer Jr JC (1983) The effects of recalculation on estimates of temperature and oxygen fugacity from analyses of multicomponent iron-titanium oxides. Am Mineral 68(5-6):586–594.

Teng LS (1996) Extensional collapse of the northern Taiwan mountain belt. Geology 24(10):949-952.

Tsao SJ (1994) Potassium-argon age determination of volcanic rocks from the Tatun volcano group. Bull Central Geol Surv 9:137-154.

Viccaro M, Giuffrida M, Nicotra E, Cristofolini R (2016) Timescales of magma storage and migration recorded by olivine crystals in basalts of the March-April 2010 eruption at Eyjafjallajökull volcano, Iceland. Am Mineral 101(1):222-230. https://doi.org/10.2138/am-2016-5365

1163 Wang KL, Chung SL, O'Reilly SY, Sun SS, Shinjo R, Chen CH (2004) Geochemical
1164 constraints for the genesis of post-collisional magmatism and the geodynamic evolution
1165 of the northern Taiwan region. J Petrol 45(5):785-1011. Doi:10.1093/petrology/egh001
1166 Wang WH, Chen CH (1990) The volcanology and fission track age dating of pyroclastic
1167 deposits in Tatun volcano group, northern Taiwan. Acta Geologica Taiwanica 28:1-30.
1168 Widiyantoro S, Ramdhan M, Métaxian JP, Cummins PR, Martel C, Erdmann S (2018)
1169 Seismic imaging and petrology explain highly explosive eruptions of Merapi Volcano,
1170 Indonesia. Sci Rep 8(1):1-7.
1171 Wright TL, Doherty PC (1970) A linear programming and least squares computer method for
1172 solving petrologic mixing problems. Geol Soc Am Bull 81:1995-2008.
1173 Yang HY, Chen CJ (1994) High-temperature oxidation of titanomagnetite in andesitic rocks
1174 of the coastal range, eastern Taiwan. J Geol Soc China 37:291-307.
1175 Yang HJ, Frey FA, Clague DA, Garcia MO (1996) Mineral chemistry of submarine lavas
1176 from Hilo Ridge, Hawaii: implications for magmatic processes within Hawaiian rift
1177 zones. Contrib Mineral Petrol 135:355-372.
1178 Yeh YH, Barrier E, Lin CH, Angelier J (1991) Stress tensor analysis in the Taiwan area from
1179 focal mechanisms of earthwuakes: Tectonophys 200:276-280.
1180 Zhang J, Humphreys MCS, Cooper GF, Davidson JP, Macpherson CG (2017) Magma mush
1181 chemistry at subduction zones, revealed by new melt major element inversion from
1182 calcic amphiboles. Am Mineral 102:1353-1367.
1183 Zellmer GF, Rubin KH, Miller CA, Shellnutt JG, Belousov A, Belousova M (2015) Resolving
1184 discordant U-Th-Ra ages: constraints on petrogenetic processes of recent effusive
1185 eruptions at Tatun Volcano Group, northern Taiwan. In: Caricchi, L., Blundy, J.D. (ed)
1186 Chemical, Physical and Temporal Evolution of Magmatic Systems. Geol Soc, London.
1187 Special Pub. 422. http://doi.org/10.1144/SP422.3

Supplementary Files

This is a list of supplementary files associated with this preprint. Click to download.

- ESM1260829.docx
- ESM2260829.xlsx